International Journal of Heat and Mass Transfer 220 (2024) 124940

Contents lists available at ScienceDirect

International Journal of Heat and Mass Transfer

journal homepage: www.elsevier.com/locate/ijhmt

# Experimental investigation of flow orientation effects on cryogenic flow boiling

Sunjae Kim [a], Dylan Foster [a], Nishad Damle [a], Issam Mudawar [a,*], Jason Hartwig [b]

[a] Purdue University Boiling and Two-Phase Flow Laboratory (PU-BTPFL), School of Mechanical Engineering, Purdue University, 585 Purdue Mall, West Lafayette, IN 47907, USA
[b] Fluids and Cryogenics Branch, NASA Glenn Research Center, 21000 Brookpark Rd, Cleveland, OH 44135, USA

ARTICLE INFO

*Keywords:*
Cryogens
Flow boiling
Flow orientation effect
Two-phase heat transfer coefficient
Bubble collision dispersion

ABSTRACT

Cryogenic flow boiling physics is of paramount importance for future cryogenic space applications employing Cryogenic Fluid Management (CFM) technologies. This experimental study investigates the two-phase flow and heat transfer performance of $LN_2$ flow boiling across five distinct flow orientations: vertical upflow, vertical downflow, horizontal flow, 45° inclined upflow, and 45° inclined downflow. The study employed the steady-state heating method within a circular heated tube featuring an 8.5-mm inner diameter and a 680-mm heated length. High-speed video recordings were utilized to capture two-phase flow patterns and interfacial behaviors across various flow orientations. The experiments covered a wide range of operating conditions, including mass velocities ranging from 351.80 to 1572.77 kg/m$^2$s and inlet pressures from 297.14 to 1032.97 kPa, primarily with near-saturated inlet subcooling. Distinct two-phase flow patterns and regime transitions were identified for each flow orientation. Symmetrical flow patterns were evident in vertical orientations, whereas non-vertical orientations exhibited asymmetric flow stratifications, primarily influenced by the buoyancy force in a terrestrial gravity environment. Bubble dynamic parameters were quantified, and bubble collision and dispersion phenomena were visualized. Analyzing heat transfer performance based on local flow boiling curves and variations in heat transfer coefficients (HTCs), it was observed that vertical upflow demonstrated the most enhanced heat transfer performance, while vertical downflow exhibited the lowest. As mass velocity exceeded 830 kg/m$^2$s, the differences in heat transfer among orientations became less distinct, emphasizing the role of flow inertia in mitigating the influence of flow orientation. A direct comparison of microgravity HTC data from a recent study by the authors against the 1-$g_e$ HTC data indicated enhanced heat transfer performance in microgravity for flow orientation configurations in terrestrial gravity. However, this enhancement progressively diminished as the heat flux increased. Distinct HTC trends were observed as mass velocity increased for different flow orientations and gravity levels.

## 1. Introduction

### 1.1. Cryogenic applications in space

Cryogenic propellants, known for their notably high performance in terms of specific impulse and energy density compared to conventional propellants, have garnered significant attention in recent years for their diverse applications, particularly for space exploration. Moreover, a recently reported NASA roadmap designated cryogenic fluid management (CFM) technologies as essential to achieving efficient utilization of cryogenic propellants for NASA's future long duration missions [1].

To further enable capacity for missions traveling far outside low Earth orbit (LEO), cryogenic fuel depot systems will be required for providing the necessary propellant for maneuvering and other in-space activities. These systems typically involve the transfer of cryogenic liquids from a large volume storage tank to smaller tanks or spacecrafts [2]. During the fuel transfer, it is crucial to ensure that the system hardware, including the feed line, flow components, and various storage tanks, be cooled down to cryogenic temperatures before providing vapor-free liquid. The cooling process is typically achieved through phase change heat transfer, where a portion of the propellant is allowed to boil, effectively removing thermal energy from the system walls [3], which highlights the importance of understanding flow boiling fluid physics of cryogens. The necessity of CFM technology is not limited to propellant transfer or storage for fuel depots but is more emphasized as a key

* Corresponding author.
*E-mail address:* mudawar@ecn.purdue.edu (I. Mudawar).

https://doi.org/10.1016/j.ijheatmasstransfer.2023.124940
Received 18 August 2023; Received in revised form 16 October 2023; Accepted 7 November 2023
Available online 15 November 2023

**Nomenclature**

| | |
|---|---|
| $A$ | area ($m^2$) |
| $D$ | diameter (m) |
| $D_b$ | bubble departure diameter (m) |
| $D_{bw}$ | diameter of bubbles attached on the wall (m) |
| $F_{BCD}$ | bubble collision dispersion force per cell volume ($N/m^3$) |
| $Fr_M$ | Froude number for a mixture; $\frac{G}{\rho_f}\left[1+x\left(\frac{\rho_f}{\rho_g}-1\right)\right](gD)^{-1/2}$ |
| $G$ | mass velocity ($kg/m^2s$) |
| $g_e$ | Earth gravity ($m/s^2$) |
| $h$ | enthalpy (J/kg); heat transfer coefficient ($W/m^2K$) |
| $h_{fg}$ | latent heat of vaporization (J/kg) |
| $k$ | thermal conductivity (W/m•K) |
| $K$ | proportionality constant |
| $L$ | length (m) |
| $L_e$ | entrance length (m) |
| $L_H$ | heated length (m) |
| $L_{sp}$ | single-phase liquid length (m) |
| $\dot{m}$ | mass flow rate (kg/s) |
| $N_{bw}$ | number of bubbles attached on the wall |
| $P$ | pressure (Pa) |
| $Q$ | total heat input [W] |
| $q''$ | wall heat flux ($W/m^2$) |
| $S$ | suppression factor |
| $T$ | temperature ( °C, K) |
| $t$ | time (s) |
| $Th$ | thickness (m) |
| $u$ | velocity (m/s) |
| $u_{bw}$ | velocity of bubble sliding on the wall (m/s) |
| $u_c$ | core velocity (m/s) |
| $u_t$ | liquid fluctuation velocity due to bubble agitation (m/s) |
| $\dot{V}$ | volume flow rate ($m^3/s$) |
| $x_e$ | thermodynamic equilibrium quality |
| $z$ | axial coordinate (m) |

*Greek symbols*

| | |
|---|---|
| $\alpha$ | void fraction averaged over flow area |
| $\alpha_{max}$ | dense packing limit |
| $\theta$ | flow orientation angle |

*Subscripts*

| | |
|---|---|
| *avg* | average |
| *b* | bubble |
| *f* | liquid |
| *g* | vapor |
| *i* | inner |
| *in* | inlet to heated tube |
| *meas* | measured |
| *nb* | nucleate boiling |
| *o* | outer |
| *out* | outlet |
| *pb* | pool boiling |
| *s* | solid tube |
| *sat* | saturation |
| *sp* | single-phase liquid |
| *sub* | subcooling |
| *w* | wall |
| *z* | local |

*Acronyms*

| | |
|---|---|
| BCD | bubble collision dispersion |
| CFD | computational fluid dynamics |
| CFM | cryogenic fluid management |
| CHF | critical heat flux |
| HTC | heat transfer coefficient |
| LEO | low Earth orbit |
| $LH_2$ | liquid hydrogen |
| $LN_2$ | liquid nitrogen |
| LOX | liquid oxygen |
| NTP | nuclear thermal propulsion |
| ONB | onset of nucleate boiling |
| ONBD | onset of departure from nucleate boiling |
| SV | solenoid valve |

technology area for developing Nuclear Thermal Propulsion (NTP) powered vehicles. NTP, whether designed to provide the thrust to move a spacecraft between orbits or operate as a dual-mode system that provides power and propulsion capability, provides strong architectural benefits to exploration missions and reusable in-space transportation systems [4]. Such NTP systems use a nuclear reactor to heat a propellant, such as $LH_2$, which is then expelled out of a nozzle to produce thrust and also used as coolant for maintaining acceptable temperature of the nuclear reactor. Consequently, the importance of understanding cryogenic flow boiling fluid physics should be highlighted in order to design high fidelity reactors and incorporated feed systems of NTP; this is equivalent to how thermal hydraulic understanding of water is crucial for pressurized water reactors (PWRs) in Earth based nuclear reactors. Additional applications where CFM technologies play a critical role include, but are not limited to, ascent and descent stages, feedlines for gas/gas or liquid/liquid engines, and superconducting hydrogen aircraft. Fig. 1 shows examples of in-space applications requiring CFM technology.

### 1.2. Unique fluid and thermal properties of cryogens

Cryogens constitute a distinct category of fluids that possess unique thermal properties which are clearly distinguishable from water and conventional refrigerants, representatively by their extremely low saturation temperature. Utilizing such low saturation temperature, cryogens are vastly adapted for various industrial applications where extreme cooling temperature has to be maintained. For example, liquid nitrogen ($LN_2$) is used to fast freeze food, preserve tissue and blood, and eliminate targeted tissue in cryosurgery, liquid oxygen (LOX) in life support systems and fuel cells, and liquid hydrogen ($LH_2$) as coolant for superconducting magnets. However, it is not only the saturation temperature that delineates cryogens from other conventional room-temperature fluids, as demonstrated in Fig. 2. Fig. 2(a) shows saturated liquid properties, including density, $\rho_f$, specific heat at constant pressure, $c_{p,f}$, thermal conductivity, $k_f$, viscosity, $\mu_f$, and Prandtl number, $Pr_f$, as a function of reduced pressure, $P_R$, ranging from 0 to 1, for different fluid classes. In Fig. 2(b), variations of relevant phase change properties for cryogens, namely vapor density, $\rho_g$, latent heat of vaporization, $h_{fg}$, and surface tension, $\sigma$, are presented as a function of $P_R$ and compared with other fluid categories. The following trends are clearly captured in Fig. 2: (a) low liquid viscosity, $\mu_f$, (b) low surface tension, $\sigma$, and (c) low latent heat of vaporization, $h_{fg}$. These unique thermophysical properties impact both fluid and heat transfer physics of cryogens which also reflects on dimensionless parameters. The exceptionally low liquid viscosity, $\mu_f$, indicates a predominance of turbulent flow with high Reynolds numbers, $Re_{fo,D}$, thereby enhancing single-phase liquid forced convection at the expense of increased pressure drop. Furthermore, the extremely low surface tension, $\sigma$, causes cryogens to acquire much higher Weber numbers, $We_{fo,D}$, compared to those for water and refrigerants, which causes initiation of nucleate boiling and critical heat flux (CHF) at lower wall superheats for cryogens. Lastly, the low latent

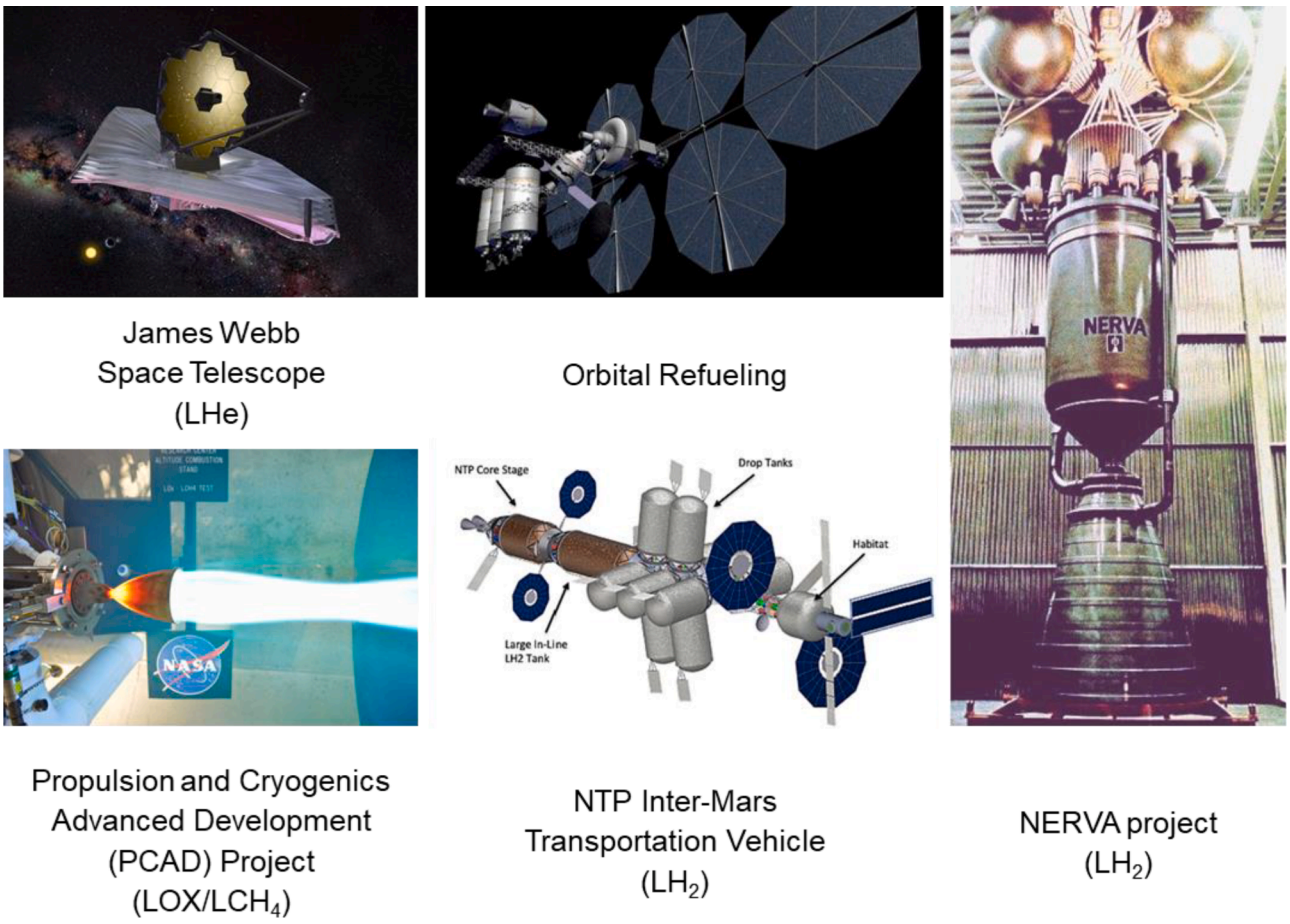


**Fig. 1.** Space applications of cryogens.

heat of vaporization, $h_{fg}$, exhibited by cryogens emphasize their high susceptibility to phase change compared to conventional room-temperature fluids under the same amount of heat load.

These distinctive thermophysical properties of cryogenic fluids significantly amplify the intricacy of comprehending the two-phase flow and heat transfer phenomena in cryogenic flow boiling. Furthermore, these unique characteristics of cryogens cast doubt on the accuracy of conventional correlations, which were originally developed based on room-temperature fluids. To illustrate this point, Hartwig et al. [3] demonstrated that conventional room-temperature HTC correlations overpredicted $LH_2$ chilldown data by a factor of up to 200. Furthermore, Mercado et al. [5] uncovered and presented evidence that conventional HTC correlations failed to accurately predict cryogenic steady-state heating data, with the maximum deviation reaching a factor of 4 between predicted and measured HTC. Given the substantial failures of the conventional correlations, and considering the unique thermal characteristics of cryogenic fluids, it is clear that cryogenic flow boiling demands special consideration.

### 1.3. Quenching method and steady state heating method

Flow boiling experiments can be performed with two different methods: (a) *steady-state heating method*, and (b) *quenching (transient) method*. Described in Fig. 3(a), using the steady-state heating method, a boiling curve is generated by initiating experiments at zero power and increasing or decreasing wall heat flux in small increments, followed each by an adequate waiting period to allow wall temperature to reach steady state before it is measured. As wall heat flux is increased in small increments, Onset of Nucleate Boiling (ONB) point and Critical Heat Flux (CHF) are identified, delineating the nucleate boiling regime. Beyond the CHF point, further increase of wall heat flux allows for capture of the upper portion of the film boiling region. To identify the Minimum Heat Flux (MHF) and the lower portion of the film boiling regime, the wall heat flux is gradually reduced until a sudden decrease in wall temperature is observed, indicating the transition to the nucleate boiling regime. However, it is worth noting that the steady-state method lacks the ability to capture the transition boiling regime of the boiling curve. The second, *quenching* method assesses transient cooling performance by introducing colder liquid flow to preheated tube or channel, which, in turn, generates a complete temperature-time (quench) curve as shown in Fig. 3(b). It is important to note that the shape of the quench curve is strongly influenced by the thermal mass of the wall. Eventually, variation of the heat flux with wall superheat for each regime is determined via transient conduction analysis of the wall, generally using a lumped mass model.

Since the quenching method is inherently transient, recorded and analyzed data inherently includes transient uncertainties. Moreover, extracting HTC data from the quenching method requires the quantification of parasitic heat leak, introducing an additional potential source of uncertainty. In contrast, the heated tube method records data under steady-state conditions after the wall temperatures stabilize under fixed heat flux. Furthermore, since the imposed heat flux is generally one or two orders of magnitude higher than the parasitic heat leak, uncertainties are typically lower for the steady-state heating method compared to quenching experiments. Therefore, the steady-state heating method is preferred in flow boiling studies due to its greater accuracy in measuring heat transfer parameters of interest.

Most prior studies on cryogenic flow boiling, despite the high uncertainties, have primarily focused on using the quenching method to examine line chilldown processes in diverse cryogenic transfer systems.

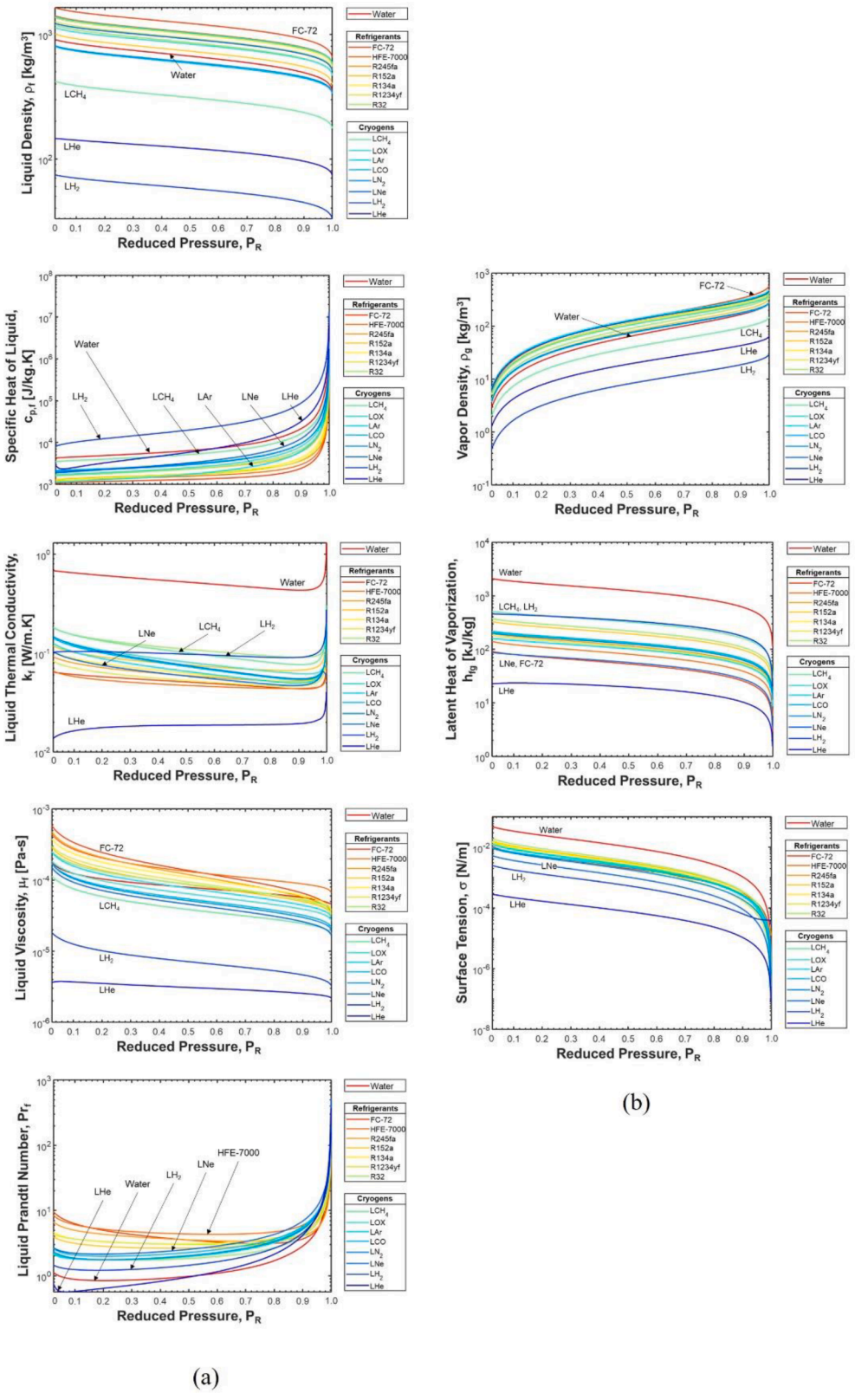


**Fig. 2.** (a) Variations of saturated liquid properties (density, specific heat at constant pressure, thermal conductivity, viscosity, and Prandtl number) with reduced pressure. (b) Variations of saturated vapor density, latent heat of vaporization, and surface tension with reduced pressure.

However, to develop precise and reliable prediction tools, such as empirical correlations for HTC and CHF for forthcoming cryogenic space applications, it becomes evident that high-accuracy HTC data are a fundamental necessity. This highlights the essential need to undertake experimental investigations for cryogenic flow boiling, employing the steady-state heating method to construct a comprehensive and high-accuracy HTC database.

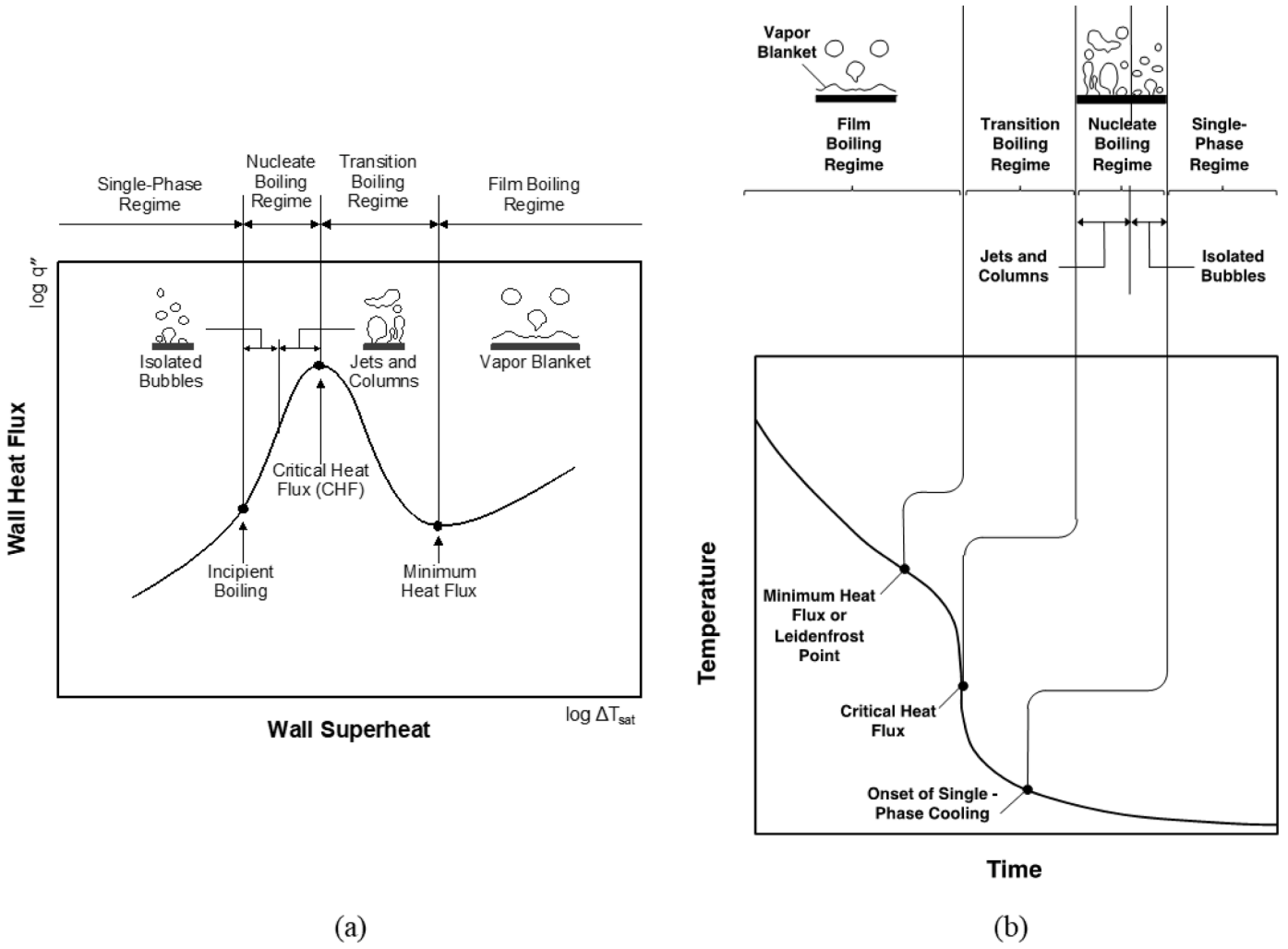


**Fig. 3.** (a) Boiling curve, generally measured using the steady-state heating method, and (b) quench curve, generally measured using the transient (quench) method; both are shown for pool boiling.

### *1.4. Experimental investigation of flow orientation effect on flow boiling physics*

Over the past several decades, flow orientation effect on flow boiling has been experimentally studied focusing on two different parameters, critical heat flux (CHF), and two-phase heat transfer coefficient (HTC). Mishima and Nishihara [6] highlighted the significance of comprehending the effect of flow orientation on water flow boiling, particularly in the context of nuclear reactor accidents that requires the removal of decay heat through natural convection. To investigate this, they designed an experimental facility with rectangular test sections featuring a clearance of 2.4 mm and a width of 40 mm, forming a thin-rectangular flow channel. They conducted a flow boiling experiment, measuring CHF for vertical upflow and vertical downflow within an operating mass velocity range of up to 700 kg/m$^2$s. The experimental results revealed that CHF was consistently higher for vertical upflow than for vertical downflow across the entire range of tested mass velocities. Similarly, but with a finer discretization of flow inclination angles, Zhang et al. [7] conducted a flow boiling experiment using FC-72, covering a wide flow velocity range from 0.1 to 1.5 m/s. They assessed the impact of flow orientation by conducting tests at various channel inclinations in increments of 45°. Notably, the lowest inlet velocity yielded the most pronounced variations in interfacial behavior, which were reflected in substantial variations in CHF for different orientations. Based on their experimental results, Zhang et al. [7] reported that the influence of flow orientation diminishes as the inlet velocity increased, and suggested a critical flow velocity of 1.5 m/s, beyond which CHF values became relatively consistent regardless of flow orientation. While the previous two studies investigated flow orientation effect on CHF, Kharangate et al. [8] conducted a flow boiling heat transfer experiment using FC-72 to analyze the influence of flow orientation on the HTC in vertical upflow, vertical downflow, and horizontal flow configurations. They designed an experimental facility featuring a rectangular channel with dimensions of 2.5 mm by 5 mm and a heated length of 114.6 mm. A wide range of mass velocities, spanning from 183.5 to 2030.3 kg/m$^2$s, was examined to identify the critical mass velocity at which the system becomes insensitive to orientation effects. Their results revealed that the most significant difference in heat transfer coefficient was observed within the lowest mass velocity range of $G$ = 200.9–235.9 kg/m$^2$s. At such low mass velocities, the heat transfer coefficients for vertical upflow and vertical downflow were nearly twice as high as those for horizontal flow. However, the influence of flow orientation on average heat transfer coefficient diminished notably as mass velocity increased. They reported that above a critical mass velocity of $G$ = 800 kg/m$^2$s, average HTC values were approximately equal for all orientations, demonstrating that inertia becomes effective in mitigating orientation effects around this mass velocity. More recently, Saisorn et al. [9] conducted similar flow boiling experiments using R-134a in vertical upflow, vertical downflow, and horizontal flow configurations. Their test section featured a circular

mini-channel with a diameter of 1 mm and a heated length of 500 mm. They compared heat transfer performance among the three different orientations and observed a hierarchy of HTCs. Specifically, they reported that vertical downflow exhibited the highest performance at a mass velocity of 252 kg/m$^2$s, followed by vertical upflow, with horizontal flow having the lowest performance. However, it should be noted that this reported hierarchy contradicts the conventional findings typically observed in macro-channels, such as the results obtained with a 12.7 mm x 12.7 mm rectangular channel from Thorncroft et al. [10], where HTCs for vertical upflow generally exhibited higher performance compared to vertical downflow.

Overall, certain generalizations can be inferred from these experimental studies using common fluids: (a) a pronounced flow orientation effect is observed at low mass velocities, (b) vertical upflow tends to exhibit superior heat transfer performance compared to other orientations, and (c) the influence of orientation diminishes at higher mass velocity conditions.

When it comes to cryogenic flow boiling, only a limited number of experimental studies have systematically explored the impact of flow orientation on cryogenic boiling heat transfer. Kawanami et al. [11] employed the quenching method to conduct $LN_2$ quenching flow boiling experiments utilizing three different flow tubes with inner diameters of 7, 10, and 13.6 mm, each having a length of 150 mm. They reported maximum and minimum heat flux measurements across a mass velocity range of 300 to 600 kg/m$^2$s for vertical upflow and downflow quenching. The study highlighted that in downward flow, the flow pattern during film boiling was exclusively characterized by filamentary flow, with no occurrence of inverted annular flow. Consequently, this absence of inverted annular flow significantly reduced the MHF in comparison to what is typically observed in upward flow configurations. However, the authors did not delve into an in-depth investigation of the associated orientation effect on HTC nor did they propose a critical mass velocity threshold to overcome the orientation-dependent effect. Darr et al. [12] conducted an extensive investigation into the influence of orientation on $LN_2$ quenching flow boiling, encompassing nine different flow orientations spanning from $+90^\circ$ to $-90^\circ$. They employed a stainless steel (SS304) tube with an inner diameter of 11.68 mm and a length of 572 mm for their experiments. A wide range of mass velocities, ranging from 5 to 1700 kg/m$^2$s, were tested, and the results were primarily presented in terms of the average HTC for both film boiling and nucleate boiling regimes. Their findings indicated that the heat transfer rate was highest for vertical upflow and lowest for vertical downflow, with the remaining inclined flow orientations falling between these two extremes. However, as the mass velocity increased and surpassed a critical mass velocity of 1600 kg/m$^2$s, the average heat transfer coefficient became independent of flow orientation. In this regime, no discernible difference in heat transfer characteristics was observed between vertical upflow and vertical downflow. The authors elucidated that the critical mass velocity of $G = 1600$ kg/m$^2$s signifies a transition point at which forced convection prevails over natural convection, resulting in both the HTC and quenching time becoming independent of flow direction. Simoneau and Simon [13] initiated a cryogenic flow boiling investigation utilizing the steady-state heating method, with a specific emphasis on visualizing interfacial behavior to examine the impact of flow orientation on the hydrodynamics of cryogenic flow boiling. They presented visual recordings of flow patterns for both vertical upflow and vertical downflow configurations under varying operating conditions. Notably, their observations revealed a pronounced buoyancy effect in the downflow orientation, particularly at low velocity of 0.26 m/s, where vapor accumulation was prominent, consequently leading to a lower CHF compared to vertical upflow. While they qualitatively suggested that the impact of flow orientation diminished at higher velocity of 0.79 m/s based on visual analysis, they did not provide a quantified comparison that would elucidate the impact of the flow orientation effect on cryogenic heat transfer performances. Klimenko et al. [14] conducted $LN_2$ flow boiling experiments using the steady-state heating method testing vertical upflow and horizontal flow configurations. The authors introduced modified Froude number, $Fr_M$, as a non-dimensionalized criterion characterizing the balance between inertial and gravitational forces. Surprisingly, their findings presented counterintuitive results, suggesting that in regions influenced by gravity, where the condition $Fr_M \leq 20$ is met, the HTCs for horizontal flow can be twice as high as those for vertical upflow. However, as the mass velocity increased to the point where $Fr_M > 40$, they proposed that flow orientation no longer exerted a significant impact on the intensity of the heat transfer coefficient. They further suggested that the HTC correlation developed by Klimenko [15] could be applied effectively to both flow orientations under such conditions.

In contrast to the generalized trends observed in experimental studies involving room-temperature fluids, the existing body of literature on cryogenic flow boiling presents contradictory trends regarding the influence of flow orientation on cryogenic flow boiling phenomena. Furthermore, as emphasized by Klimenko et al. [14], the current cryogenic HTC database significantly lacks comprehensive information regarding direct comparisons of HTC across multiple flow orientations. The data gaps in the cryogenic database are further underscored and clearly identified by Ganesan et al. [16], as follows:

(1) Additional data for accurate local HTC acquired by steady-state heating method
(2) Additional data for local HTC with flow orientations other than vertical upflow and horizontal flow
(3) Additional data for local HTC with high mass velocities
(4) Additional data for local HTC for large length-to-diameter ratios

Hence, to rectify the identified knowledge gap within the cryogenic flow boiling database, it is essential to undertake flow boiling experiments encompassing various flow orientations. These experiments should employ a steady-state heating method and encompass a broad spectrum of operating conditions, ranging from low to high mass velocities, while employing relatively large length-to-diameter tubes as heated test sections.

### 1.5. Objectives of present study

This study presents results obtained from steady-state heated tube cryogenic flow boiling experiments using $LN_2$ as the working fluid. The experiments were carried out under Earth's gravity and encompassed multiple flow orientations, including vertical upflow, vertical downflow, horizontal flow, 45° inclined upflow, and 45° inclined downflow. The experiments were performed using the same cryogenic payload that was constructed for parabolic flight experiments and employed in the authors' prior experimental studies [17,18]. The primary objective of these experiments was to systematically collect and acquire $LN_2$ two-phase heat transfer data using the steady-state heating method across various flow orientations, which has been identified as a knowledge gap among the current body of cryogenic literature. Additionally, high-speed video recordings were employed to capture and analyze interfacial behavior, thereby supplementing the heat transfer data with a comprehensive understanding of the fluid physics involved in flow boiling. Furthermore, recorded flow image sequences were closely examined and revealed the specific bubble dynamics of bubble collision dispersion phenomena. These phenomena were experimentally observed and captured in three distinct flow orientations, providing empirical evidence that validated the CFD simulated prediction of the phenomenon. Heat transfer results are presented in the form of local boiling curves, local and average heat transfer coefficients for the five different flow orientations. The newly acquired data are compared with previously measured microgravity data [17] to expand the comprehension of body force effects on flow boiling physics, not only of the influence of flow orientation but also of the gravitational field. The effects of mass velocity on both local and average heat transfer coefficients

is analyzed for each flow orientation, revealing distinct trends in heat transfer characteristics as the mass velocity varies.

This study will provide the most comprehensive assessment to date on the effects of flow orientation, microgravity, and mass velocity on cryogenic flow boiling with near-saturated inlet conditions. The accumulated experimental database will serve as the basis for developing prediction tools for cryogenic flow boiling, such as empirical correlations, analytical models, and/or CFD models.

## 2. Experimental methods

### 2.1. Experiment facility

#### 2.1.1. Two-phase flow loop

Fig. 4 illustrates a schematic of the open-loop two-phase flow system utilized to (i) provide working fluid, $LN_2$, into the test section and (ii) safely vent fluid from the test section outlet to ambient air. Even though the experimental facility has been thoroughly documented in Kim et al. [18], a brief summary is provided herein to help understanding of the obtained results.

Since the loop is designed as an open circuit, a nitrogen gas cylinder with a volume of 44 L, which is initially pressurized to 14.5 MPa, is connected to the $LN_2$ dewar to provide positive ullage pressure and displace the $LN_2$ from the dewar. A turbine flow meter is employed to measure the volume flow rate of the liquid. For accurate determination of the mass flow rate, fluid density information is necessary. To obtain precise thermal property values for the incoming liquid, the temperature and pressure of the fluid are measured immediately downstream from the flow meter. The liquid then enters the test section, where a finite amount of heat is added, causing the fluid to undergo phase change and emerge as a two-phase mixture. At the outlet of the test section, fluid temperature and pressure are measured at the same axial location. The fluid is then directed into an adiabatic visualization chamber utilizing a transparent Pyrex tube, which permits interfacial behavior to be captured with the aid of a high-speed video camera (additional design details relating to the test section and visualization chamber are provided in a later section). To regulate the flow rate, a cryogenic grade needle valve is installed downstream of the visualization section. The needle valve allows for precise control of the fluid's mass velocity by sensitively adjusting the vertical movement of the needle through 11 rotations, ranging from fully open to fully closed. Two 3-kW rated vent heaters are serially connected downstream of the needle valve to

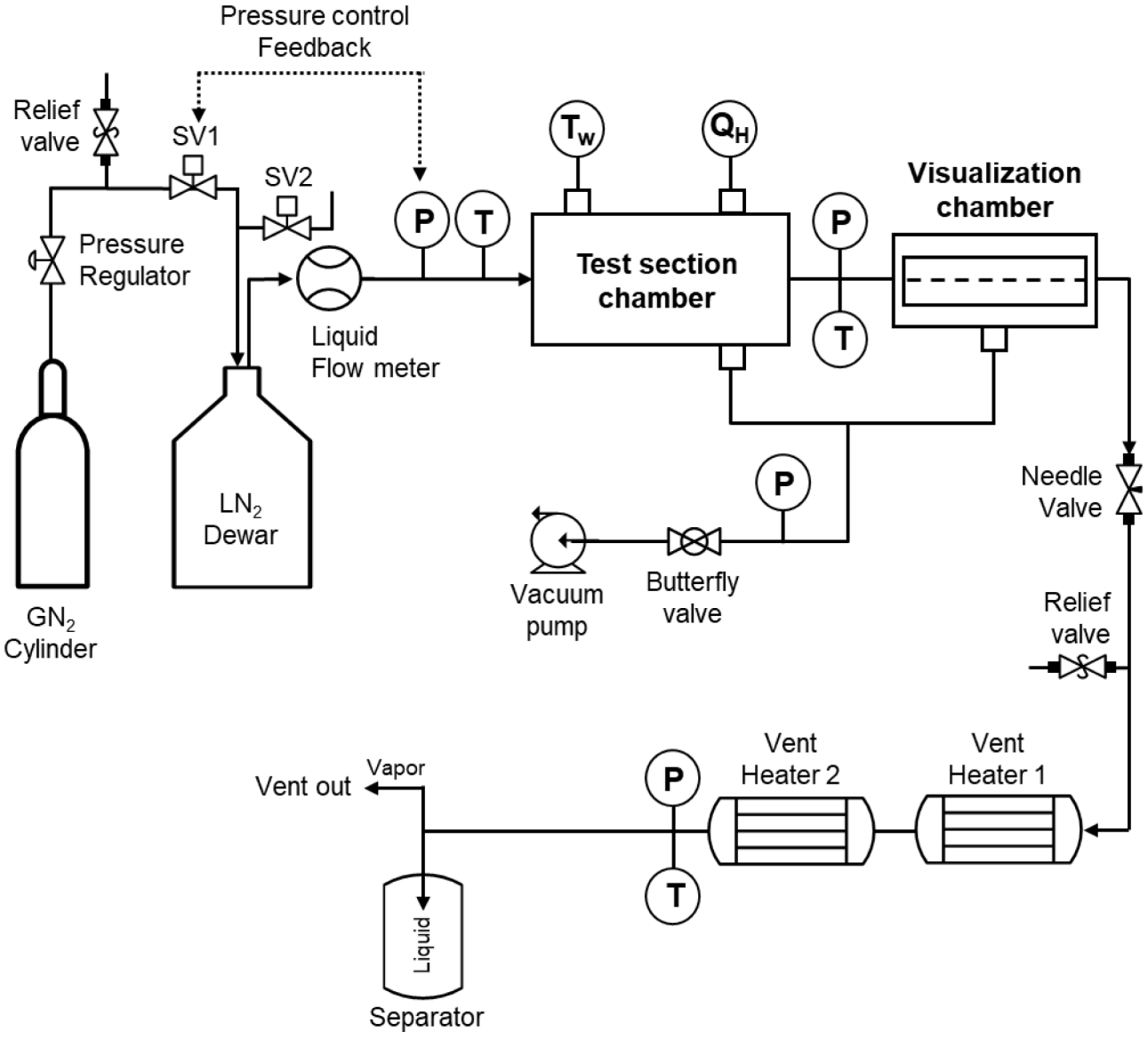


**Fig. 4.** Schematic of two-phase flow loop.

completely evaporate any remaining two-phase mixture to pure vapor phase. At the outlet of the second vent heater, fluid temperature and pressure are measured. Farther downstream, the flowline is connected to a receiver tank which serves to eliminate any possibility of liquid escaping outboard in improbable situations such as vent heater power loss. Finally, during ground testing, the vapor is safely discharged through a vent hose to the ambient environment.

*2.1.2. Constructed test facility and rotating mechanism*

Fig. 5(a) presents a 3D CAD drawing of the flight payload, illustrating all the flow components integrated into the setup. The rig is built upon a 12.7-mm thickness aluminum (AL7075-T6) baseplate with carved out hollow interior (to reduce weight when testing in parabolic flight) and an 80/20 aluminum structure to ensure structural integrity of the entire setup. The flow loop is positioned in the lower middle part of the payload. To prevent any secondary flow effects caused by variations in hydrostatic pressure, the piping is maintained at the same elevation from the inlet of the test section to the inlet of the vent heater. The dewar is positioned in the back-right cubicle with rails upon which the dewar can be easily installed or removed. Two vacuum chambers, one surrounding the test section and another the visualization chamber, are strategically positioned near the system operators at the front of the payload. The vent heater assembly is stationed in the back-left corner on the middle plane of the payload as a U-shaped tubing fitted with 20 individual nozzle heaters producing 6 kW in total. The control console of the payload is situated in the bottom-left corner of the rig. The control console integrates all electronic devices, including a data logger, AC power distributors, a DC power converter, circuit breakers, heater power controllers for test section heaters, heater temperature controllers for vent heaters, power meters for heaters, and an Arduino board for pressure automation control. All the controlled and measured parameters are integrated through LabVIEW software and displayed on a monitor installed on the front of the control console. Fig. 5(b) showcases an actual photograph of the payload.

A modular testbed was constructed to enable experimentation at different flow orientations. As shown in Fig. 5(c), the rotating facility was designed to mount the test section and visualization section, while preserving all other components of the flow loop in place on the main facility. Fig. 5(d) shows a CAD schematic of the rotating facility integrated with the rest of the flow loop. The rotating mechanism enabled orientation testing at 45° increments to allow for vertical upflow, vertical downflow, horizontal flow, 45° inclined upflow, and 45° inclined downflow. This was accomplished by installing an aluminum shaft at the center of a mounting platform for the test/visualization sections. The platform was supported by, and rotated along, two shaft bushings located on an outer supporting structure. The desired orientation is

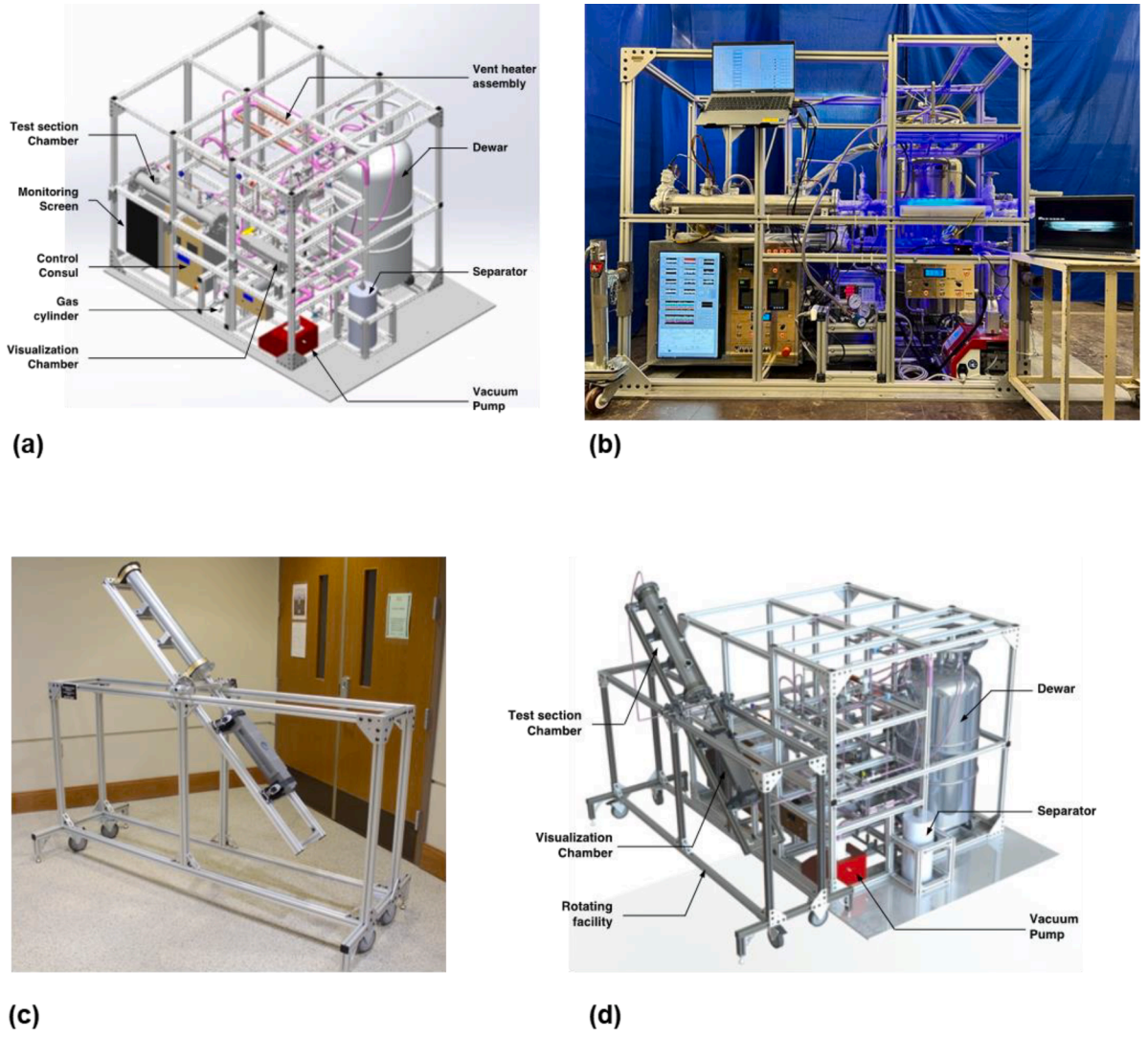


**Fig. 5.** (a) 3D CAD model, (b) picture of the experimental facility, (c) Picture of the rotating facility, and (d) 3D CAD model of the integrated facility for orientation experiments.

achieved by locking a pair of steel pins into a circular orientation guide welded to the platform's shaft.

*2.1.3. Heat transfer test section and visualization section*

The primary components of the payload are the test section and the visualization section. The test section is comprised of a heated tube that is enclosed within a vacuum chamber serving to minimize heat loss. As shown in Fig. 6(a), the vacuum chamber has an inner diameter of 0.1 m and length of 0.8 m and is fitted with flanges on both ends to ensure vacuum tight enclosure. A center hole is machined through each flange for insertion of the heated test section. The vacuum chamber is equipped with four feedthrough ports, three are vertical and one horizontal. The two vertical feedthroughs near to the outlet are for vacuum hose connections while the foremost vertical feedthrough passes wires from the thermocouples attached to the outer wall of the test section to an external control box containing the data logger. The horizontal feedthrough passes heater power leads from the test section's eight individual heaters. The test section assembly is comprised of a heating tube, eight individual heaters, and thermocouples wires. The test section heated tube is a thin walled ($Th = 0.5$ mm) stainless steel (SS304) tube with i.d. of $D_i = 8.5$ mm, heated length $L_H = 0.68$ m, and entrance length $L_e = 0.112$ m. To preserve the developed flow structure, the inner flow diameter of 8.5 mm is maintained from the inlet of the test section to the outlet of the visualization section. Eight individual electrically powered coil heaters, depicted schematically in Fig. 6(a), surround the test section's heated tube to provide uniform heat flux along the tube wall. At 120 VAC power input, each heater can dissipate up to 400 W, for total capacity for the eight heaters of up to 3200 W. Seven pairs of thermocouples are attached to the heated tube wall at seven axial locations, one in each pair is mounted at the top and a second at the bottom. Detailed axial locations of the thermocouples are provided in table form in 5(a). Aside from using vacuum to minimize heat loss, the entire test section assembly is wrapped with layers of insulation which are covered with aluminum sheet to minimize loss by radiation.

Shown schematically in Fig. 6(b), the visualization section is comprised of an adiabatic glass tube enclosed in a visualization vacuum chamber. The tube is made of Pyrex glass and fitted on one end with flexible metal bellows to accommodate thermal expansion as captured in Fig. 6(b). The adiabatic glass tube has outer diameter of $D_o = 9.5$ mm and length of 364.2 mm. The vacuum chamber, which is intended to minimize heat transfer to the glass tube, features rectangular stainless-steel construction with inlet and outlet flanges on both ends to ensure tight vacuum enclosure. As shown in Fig. 6(b), transparent glass windows are attached to opposite lateral sides providing a visualization length of 0.25 m; one window is used for video camera viewing and the other for backlight illumination.

Vacuum in both the test section chamber and visualization chamber is achieved by connecting both to a vacuum pump equipped with both a turbopump and a multistage diaphragm pump to achieve $10^{-5}$ hPa.

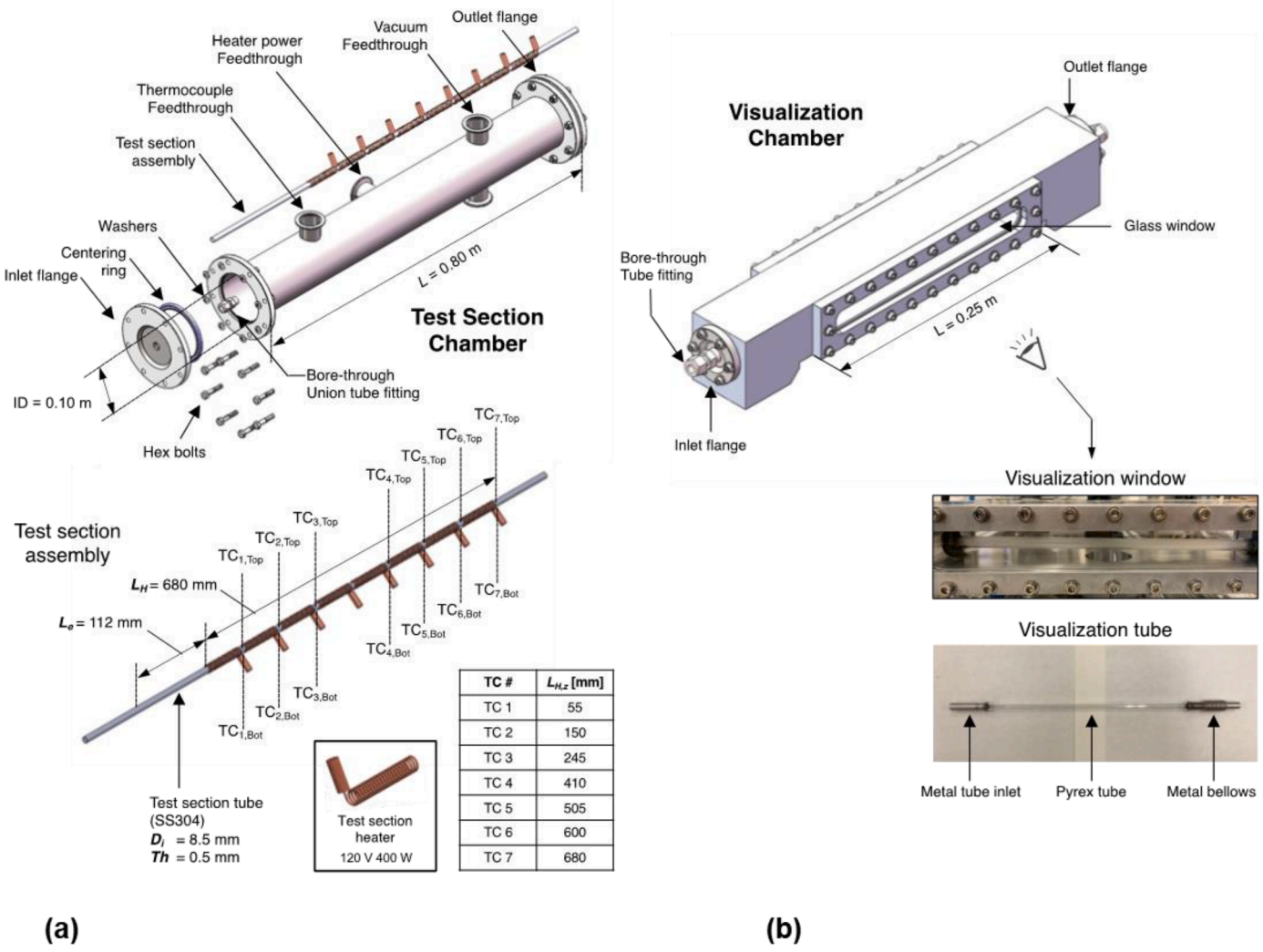


**Fig. 6.** Schematics of (a) test section chamber and assembly, and (b) visualization chamber with pictures of visualization window and Pyrex tube.

### 2.2. Instrumentation and measurement accuracy

As depicted in Fig. 6(a), two pairs of 7 type-E thermocouples are installed on the outer surface of the heated tube to enable axial wall temperature measurements. Three additional type-E thermocouples extend into the flow to measure local fluid temperature at test section inlet, test section outlet, and vent heater outlet. Local pressure measurements are obtained using four Omega Engineering absolute pressure transducers placed at the test section inlet, test section outlet, vent heater outlet, and vacuum pump inlet. Two turbine flow meters are utilized to measure flow rate. The liquid flow meter, located upstream of the test section, has a range of $1.01 \times 10^{-2}$ to $5 \times 10^{-1}$ L/s while the downstream vapor flow meter is rated for $9.4 \times 10^{-1}$ to 7.1 L/s. The measured volume flow rate is converted into mass flow rate utilizing liquid or vapor density information obtained from temperature and pressure sensors mounted in close proximity to the respective flow meter. The three test section heaters, vent heater 1, and vent heater 2 are powered by three separate power circuits to maintain electrical current for each below the allowable limit. A circuit breaker in each power circuit guards against any unintended power trip in the corresponding panel. Test section heater power input, a crucial control parameter for the flow boiling experiments, is measured using Yokogawa WT310 high accuracy power meter. All temporal temperature, pressure, flow meter, and power meter signals are acquired and recorded using a National Instruments data acquisition system (DAQ) at a sampling rate of 80 Hz. The collected temporal data are processed and analyzed using LabVIEW software and are displayed in real-time on the front monitor of the payload. Maximum uncertainties in measurements of relevant parameters are given in Table 1.

From the measurement uncertainties reported in Table 1, uncertainty propagation is analyzed and the maximum uncertainty in heat transfer coefficient is estimated using the root mean square method. Within the present database, the majority of cases exhibited uncertainty in $h_{tp,z}$ that remained below 10 %, as visually represented in Fig. 7(a). This figure clearly depicts a discernible disparity in uncertainty between the subcooled and saturated HTC datasets, with the latter exhibiting a lower level of uncertainty. Additionally, Fig. 7(b) demonstrates a notable reduction in uncertainty for $h_{tp,avg}$ as the wall heat flux increases, attributed to the simultaneous rise in wall superheat within the high wall heat flux region. Overall, the uncertainty in the majority of the $h_{tp,avg}$ dataset remains below 20 %. Note that the reported uncertainty evaluations were conducted by following the procedure introduced by O'Neil et al. [19], but modified for flow boiling measurements.

### 2.3. Flow visualization

The dynamic interfacial behavior and structures of the two-phase flow are meticulously captured in the adiabatic visualization section by employing a high-speed video camera at each steady state point along the boiling curve and at critical heat flux (CHF). Note that the adiabatic nature of the visualization section ensures that the captured flow structure is preserved from the outlet of the test section to the outlet of the visualization chamber. A high-speed video camera from Sentech is utilized and positioned to face one of the visualization chamber's windows. Meanwhile, the opposite window is backlit with blue light emitting diodes (LEDs) to minimize heat leak into the section. A light diffusing film is used to ensure uniform light intensity over the entire viewing length of the visualization chamber. The video camera can capture images with 2040×350 (*HxW*) pixel resolution at 1000 frames/s and with shutter speed of 25.8–45 μs. A single captured video image sequence consists of 250 frames or about 250 ms of flow visualization data per steady state point. Additional experimentation was conducted focusing on flow visualization using a Photron Fastcam Ultima APX high-speed camera. The camera's larger form factor did not render it suitable for previous $\mu g$ experimentation, but infrastructure modifications using the rotation facility on the ground enabled capturing interfacial behaviors with higher fidelity and speed. The videos captured were recorded at 6000 frames/s with a resolution of 512 × 512 pixels backlit by a Arrilux lamphead. These images were captured within the center of the flow visualization chamber and provide a clearer view of certain aspects of the flow dynamics, which, ultimately, facilitated the physical capturing of bubble collision and dispersion phenomena. It is noted that all high-speed video images reported in this paper have been uniformly post-processed to render flow features more distinct.

**Table 1**
Measurement uncertainties.

| Parameter | Maximum Uncertainty |
|---|---|
| Fluid temperature, $T_f$ | ±0.5℃ |
| Wall temperature, $T_w$ | ±0.5℃ |
| Volume flow rate, $\dot{V}$ | ±0.1 % reading |
| Absolute Pressure, $P$ | ±0.25 % reading |
| Heat input, $Q$ | ±0.25 % reading |

### 2.4. Data processing and experimental ranges

Steady state data are extracted from recorded temporal data by identifying each heater increment and confirming wall temperature reaching steady state. Extracted temporal data are averaged for each steady state period. Necessary thermophysical properties for nitrogen are retrieved from NIST-REFPROP [20].

Test section inlet enthalpy is found based on measured inlet temperature, $T_{in}$, and inlet and pressure, $P_{in}$, as

$$h_{in} = h(T_{in}, P_{in}) \tag{1}$$

Test section local enthalpy, $h$, at any $z$ location from the heated inlet, and outlet enthalpy, $h_{out}$, are both calculated by application of energy conservation,

$$h(z) = h_{in} + \frac{q'' \pi D_i z}{G\left(\pi D_i^2/4\right)} \tag{2a}$$

$$h_{out} = h_{in} + \frac{q'' \pi D_i L_H}{G\left(\pi D_i^2/4\right)} \tag{2b}$$

Local thermodynamic equilibrium quality, $x_{e,z}$, is calculated according to the relation

$$x_{e,z} = \frac{h - h_f\big|_P}{h_{fg}\big|_P} \tag{3}$$

where $h_f$, and $h_{fg}$ are, respectively, saturated liquid enthalpy, and latent heat of vaporization corresponding to local pressure which is linearly interpolated between measured inlet pressure, $P_{in}$ and outlet pressure, $P_{out}$.

Local fluid temperature is determined based on the following relations:

$$T_{f,z} = \begin{cases} T_{in} + \left(T_{sat}\big|_{xe=0} - T_{in}\right)\dfrac{Z}{L_{sp}} & x_{e,z} < 0 \\ T_{sat,z} & 0 \le x_{e,z} \le 1 \end{cases} \tag{4}$$

where $L_{sp}$ is the heated single-phase length, which is calculated as

$$L_{sp} = \frac{G\left(\pi D_i^2/4\right)}{q'' \pi D_i}\left(h_f\big|_{P_{in}} - h_{in}\right) \tag{5}$$

The local heat transfer coefficient (HTC) is defined based on measured local wall temperature and calculated local fluid temperature for each axial location,

$$h_z = \frac{q''}{\left(T_{w,z} - T_{f,z}\right)} \tag{6}$$

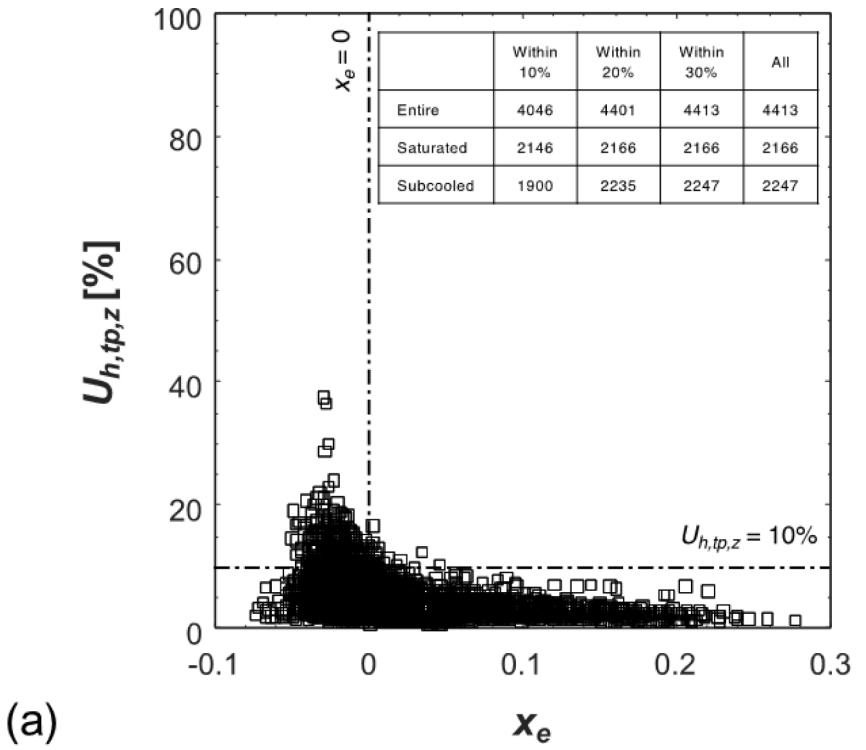


| | Within 10% | Within 20% | Within 30% | All |
|---|---|---|---|---|
| Entire | 4046 | 4401 | 4413 | 4413 |
| Saturated | 2146 | 2166 | 2166 | 2166 |
| Subcooled | 1900 | 2235 | 2247 | 2247 |

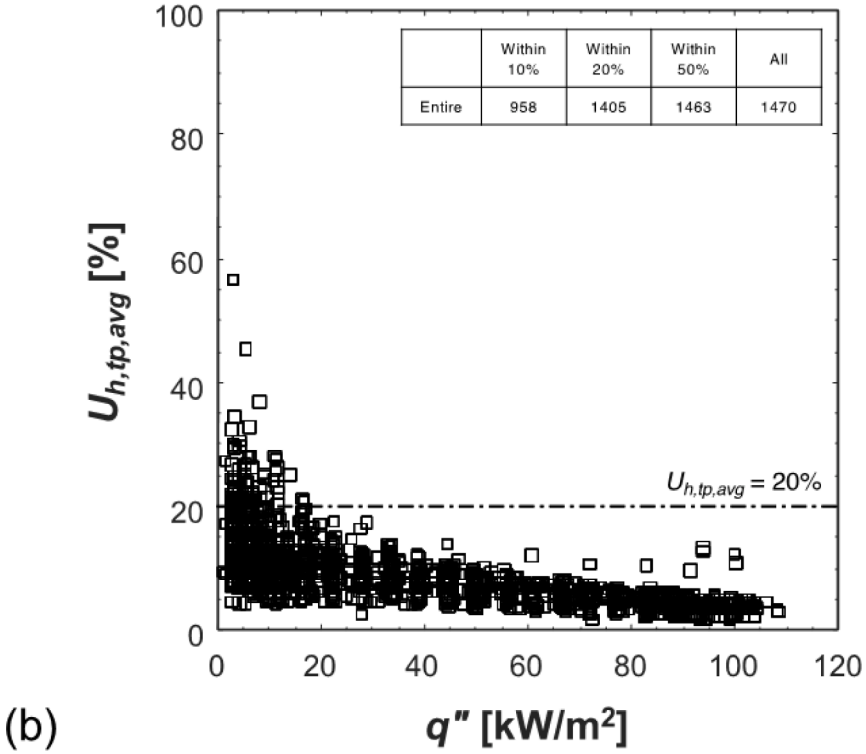


| | Within 10% | Within 20% | Within 50% | All |
|---|---|---|---|---|
| Entire | 958 | 1405 | 1463 | 1470 |

**Fig. 7.** (a) Uncertainty in local HTC with respect to equilibrium quality. (b) Uncertainty in average HTC with respect to wall heat flux.

Local inner wall temperature, $T_{w,z}$, at each axial thermocouple location is determined from measured outer wall temperature, $T_{w,o,z}$, and measured heat flux, $q''$, by accounting for conduction resistance across the heated tube wall,

$$T_{w,z} = T_{w,o,z} - \frac{q'' \pi D_i \ln(D_o/D_i)}{2\pi k_s} \tag{7}$$

The average HTC is calculated using the relation

$$\overline{h} = \frac{\iint dA}{\iint \frac{1}{h_z} dA} \tag{8}$$

which is based on harmonic averaging as proven by Ganesan et al. [16] for a constant wall heat flux boundary.

Ranges of key operating conditions for the study are summarized in Table 2.

## 3. Flow visualization results and discussion

### 3.1. Flow visualizations

From Figs. 8–12, flow visualization results for five different flow orientations are exhibited. As explained earlier, all the presented flow visualization results are captured from the adiabatic visualization section which is located just downstream from the uniformly heated test section. Flow and gravitational acceleration direction are indicated at the top of each figure, along with operating conditions: mass velocity, inlet pressure, inlet subcooling, and also magnitude of CHF. Included for each set of operating conditions are high-speed video images recorded at steady state for indicated increasing values of heat flux from above onset of boiling (ONB) until (and including) CHF. Wall heat flux, $q''$, is indicated either as kW/m$^2$ value where CHF could not be reached, Figs. 11 and 12, or as percentage of $q''_{CHF}$, which is defined as

$$\%\ CHF = \frac{q''_{meas}}{q''_{CHF}} \times 100\ [\%] \tag{9}$$

#### 3.1.1. Vertical upflow

Fig. 8 presents two-phase flow structure and flow patterns captured for $G$ = 576.8 kg/m$^2$s, $P_{in}$ = 628.8 kPa, $\Delta T_{sub,in}$ = 2.28 K in vertical upflow configuration. The objective in presenting this figure is to investigate the flow regime transitions, interfacial structures, and interfacial behaviors for this configuration. At 6 % $q''_{CHF}$, the observed flow pattern is bubbly, wherein small-sized bubbles are uniformly distributed along both the axial and radial directions. Note that in 1-$g_e$ vertical upflow, no stratification of flow patterns occurs due to the parallel alignment of the gravity vector and the flow direction. A noticeable distinction in bubble sizes is evident, with larger bubbles occupying the central core of the flow, while smaller bubbles are predominantly found in the vicinity of the tube wall. With the aid of buoyancy force and shear lift force, nucleated bubbles detach from the heated wall and migrate towards the center core. On the course of migration, bubbles grow in size by coalescing with other migrating small bubbles. Notice the bubbles attached to the wall, as indicated with the red boxes. This implies that in vertical upflow configurations, bubbles exhibit a sliding motion along the heated wall prior to complete detachment. This observation aligns with the visual recordings obtained by Thorncroft et al. [10] in their vertical upflow FC-87 flow boiling experiments, where they accredited the bubble sliding in vertical upflow for enhancing heat transfer efficiency. The enhancement of heat transfer coefficient in vertical upflow compared to other flow orientations are further examined in later sections. As heat flux increases, captured vapor structures are larger in size. From 8 % $q''_{CHF}$ to 12 % $q''_{CHF}$, the observed flow patterns are slug flow, characterized by elongated vapor bubbles flowing along the center of the tube, surrounded by numerous smaller bubbles. The increased generation of vapor bubble along the heated test section leads to a higher population of bubbles, resulting in more pronounced bubble coalescence and the formation of larger bubbles, or slug flow bubbles. The tails of these oblong bubbles are deformed due to the presence of tail wake, which causes the trailing interface to curl up and induces accumulation of smaller bubbles at the center of the vapor structure. This can be noticed from the clustered smaller bubbles following the large center vapor structure at 12 % $q''_{CHF}$. With further increase of heat flux, the distance between the large oblong bubbles decreases, resulting in flow regime transition from slug to churn, occurring amid the heat flux range of 14 to 39 % $q''_{CHF}$. As the large oblong bubbles coalesce with each other, an elongated vapor column with a turbulent vapor-liquid interface is formed, spanning the entire section of visualization. Strong shear stress is induced by the substantial disparity in phase velocities between center vapor and annular liquid, causing the interface to undergo drastic deformation and to break off small vapor fragments. From 56 % to 100 % $q''_{CHF}$, annular flow is observed having thick vapor core at the center of the tube and annular liquid film with wavy liquid-vapor interface.

The described flow patterns can be further analyzed based on classical nucleation theory. Notably, two interesting features emerge from the examination of the acquired flow images at heat flux levels of 6 % $q''_{CHF}$ and 8 %. First, there is a significant increase in the bubble population as the heat flux escalates from 6 % to 8 % $q''_{CHF}$. This observation can be ascribed to the elevated wall superheat encountered at higher heat flux conditions, consequently leading to the activation of a greater number of nucleation sites and, in turn, resulting in an augmented bubble population. The observed trend of a growing bubble population with a rise in wall superheat closely conforms to the classical nucleation theory, as elucidated by Blander and Katz [21]. In their work, they proposed a model for the rate of bubble formation per unit time per unit volume, denoted as $J$. According to their theoretical framework, the rate of bubble formation exhibits remarkable sensitivity to temperature variations, potentially increasing by up to three to four orders of magnitude with a mere one-degree Celsius temperature elevation. Second, as the heat flux increases from 6 % to 8 % $q''_{CHF}$, a notable reduction in the size of bubbles adhering to the wall becomes evident. This observation is in line with the findings of Bogojevic et al. [22], who documented a diminishing trend in bubble departure diameter as wall heat flux increased during their microchannel flow boiling experiments. They ascribed this trend to a simultaneous decrease in surface tension, leading to a higher bubble frequency, ultimately resulting in a reduction in bubble departure diameter. Further quantification and discussion of bubble dynamics will further be discussed in Section 3.1.5.

Upon closer examination of the images in Fig. 7, another intriguing feature comes to light. Even at high heat flux conditions reaching up to 86 % $q''_{CHF}$, bubbles continue to be observed within the thin annular liquid film. It is interesting that bubble nucleation can persist until such high heat flux percentages without complete suppression. As the annular regime begins to take place, any wall superheat upstream, which might

**Table 2**
Summary of key parameters of the cryogenic flow boiling experiment database.

| | Cryogenic Flow Boiling Experiment | | | | | |
|---|---|---|---|---|---|---|
| Reference | Vertical Up | Vertical Down | Horizontal | 45° Up | 45° Down | Microgravity |
| Mass flow rate, $\dot{m}$ [kg/s] | 0.02 – 0.05 | 0.03 – 0.07 | 0.02 – 0.09 | 0.02 – 0.06 | 0.02 – 0.05 | 0.02 – 0.07 |
| Mass velocity, $G$ [kg/m$^2$s] | 396.35 – 937.73 | 462.28 – 1154.70 | 406.76 – 1572.77 | 351.80 – 1100.66 | 420.76 – 941.68 | 362.13 – 1342.86 |
| Pressure, $P$ [kPa] | 389.9 – 1032.97 | 371.52 – 690.74 | 297.14 – 498.55 | 368.76 – 887.62 | 379.48 – 554.51 | 399.04 – 737.31 |
| Inlet subcooling, $\Delta T_{sc}$ [K] | 0.1 – 3.7 | 1.0 – 4.3 | 0.6 – 4.4 | 0.1 – 3.2 | 0.6 – 3.3 | 1.0 – 5.7 |
| Saturation temperature, $T_{sat}$ [K] | 90.9 – 104.3 | 90.4 – 98.3 | 87.8 – 94.0 | 90.3 – 101.9 | 90.6 – 95.3 | 91.2 – 99.2 |
| Quality, $x_e$ | −0.05 – 0.28 | −0.05 – 0.24 | −0.05 – 0.19 | −0.04 – 0.23 | −0.04 – 0.22 | −0.07 – 0.12 |
| Heat flux, $q''$ [kW/m$^2$] | 1.39 – 103.95 | 2.46 – 104.29 | 1.60 – 105.97 | 2.74 – 108.56 | 2.72 – 101.85 | 2.76 – 100.37 |

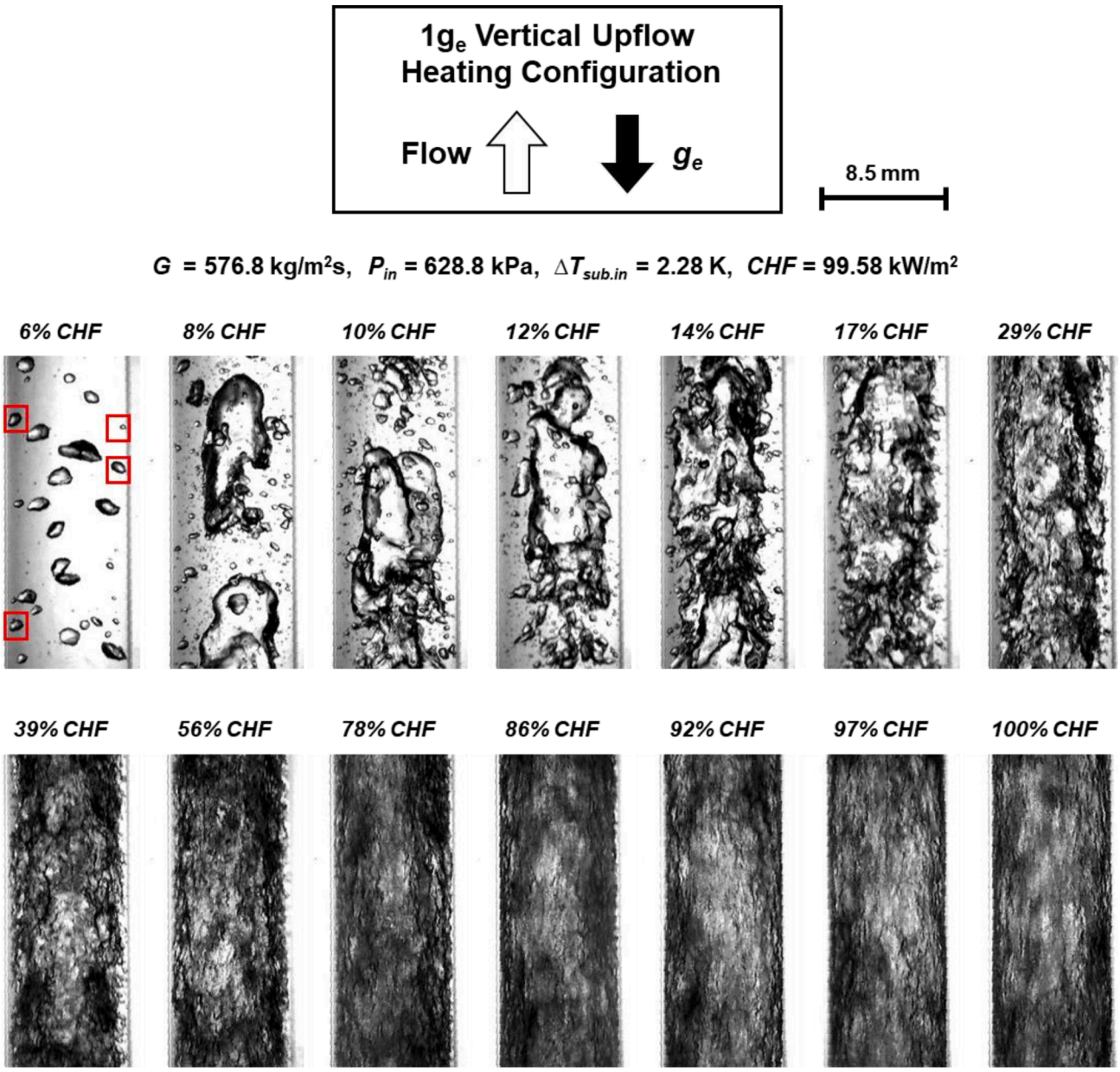


**Fig. 8.** Two-phase flow structure development along the boiling curve for vertical upflow configuration at mass velocity of $G = 576.8$ kg/m$^2$s, inlet pressure of 628.8 kPa, and inlet subcooling of 2.28 K.

have been sufficient to sustain bubble nucleation, starts to diminish due to turbulent convection in the annular liquid film [16]. As the wall temperature decreases and falls below the onset of nucleate boiling temperature, $T_{w,ONB}$, nucleate boiling ceases to exist in the annular regime. This suppression of nucleate boiling marks a transition point in heat transfer mechanism for the annular flow regime, where convective boiling takes over as the dominant heat transfer mechanism. However, in the context of cryogenic flow boiling, bubble nucleation persists even at reduced wall superheat levels within the annular flow. This persisting bubble nucleation is attributed to the unique properties of cryogens, low surface tension and low latent heat of vaporization, allowing bubble nucleation to occur even with minimal wall superheat. This ongoing bubble nucleation within the annular liquid film serves as an additional heat transfer mechanism, complementing convective heat transfer and interfacial evaporation. The combination of sustained nucleate boiling, convective boiling, and interfacial evaporation contributes to the sustained heat transfer efficiency exhibited by cryogens at higher heat flux levels. Further details regarding the associated heat transfer mechanisms and the trend of nucleate boiling suppression in $LN_2$ flow boiling will be further discussed in subsequent sections based on acquired HTC data.

### 3.1.2. *Vertical downflow*

Fig. 9 presents two-phase flow structure and flow patterns captured for $G = 511.1$ kg/m$^2$s, $P_{in} = 458.5$ kPa, $\Delta T_{sub,in} = 0.95$ K in vertical downflow configuration. At 6 % $q''_{CHF}$, the observed flow pattern is bubbly. Unlike the bubbly flow in vertical upflow configuration, here the bubbles exhibit a more pronounced alignment along the centerline of the tube. Oshinowo and Charles [23] conducted vertical downflow air-water two-phase flow experiments and also reported a similar flow pattern characterized by a core of dispersed bubbles, which they referred to as *"coring-bubbly flow"*. Moreover, due to the opposite buoyancy force vector acting against flow direction results in the axial compression of vapor bubbles, assuming disk-like shape. Notably, at such low heat flux, almost no bubbles are observed to be attached to or sliding along the wall, underscoring the effect of the buoyancy force in vertical downflow, which enhances the lift-off of bubbles from the wall.

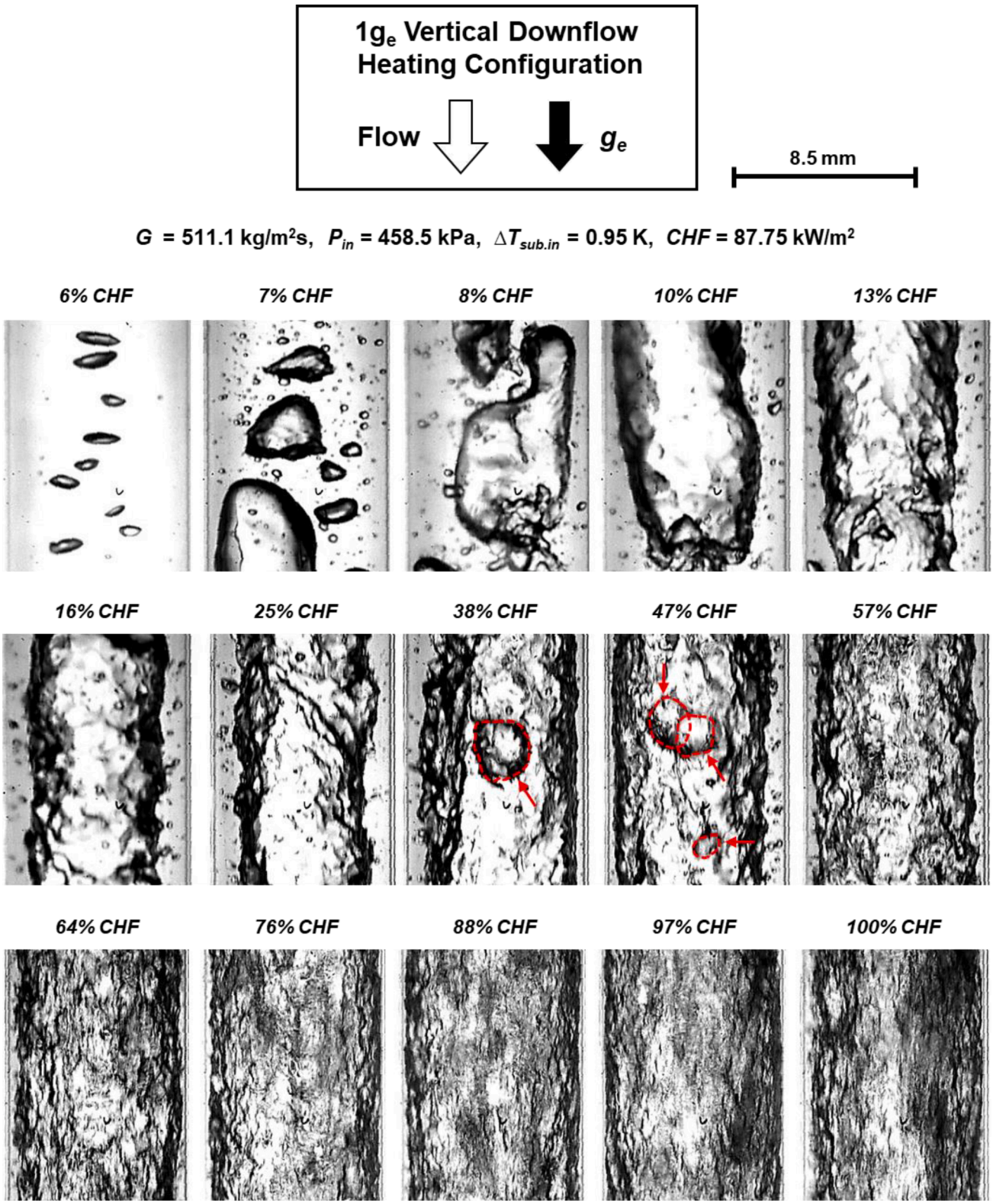


**Fig. 9.** Two-phase flow structure development along the boiling curve for vertical downflow configuration at mass velocity of $G = 511.1$ kg/m$^2$s, inlet pressure of 458.5 kPa, and inlet subcooling of 0.95 K.

This observation aligns with the visual recordings obtained by Thorncroft et al. [10] in their vertical downflow FC-87 flow boiling experiments, where they found bubbles to lift-off without or less amount of sliding along the wall. They reported bubble sliding against the flow direction can also occur in vertical downflow at extremely low flow rates. However, in the present study, it was observed that the direction of bubble sliding was parallel to the flow direction, and the reverse sliding of bubbles was not observed. The primary reason for this difference is the variation in mass velocity conditions. In the captured flow images in Fig. 9, the mass velocity was $G = 511.1$ kg/m$^2$s, whereas it was

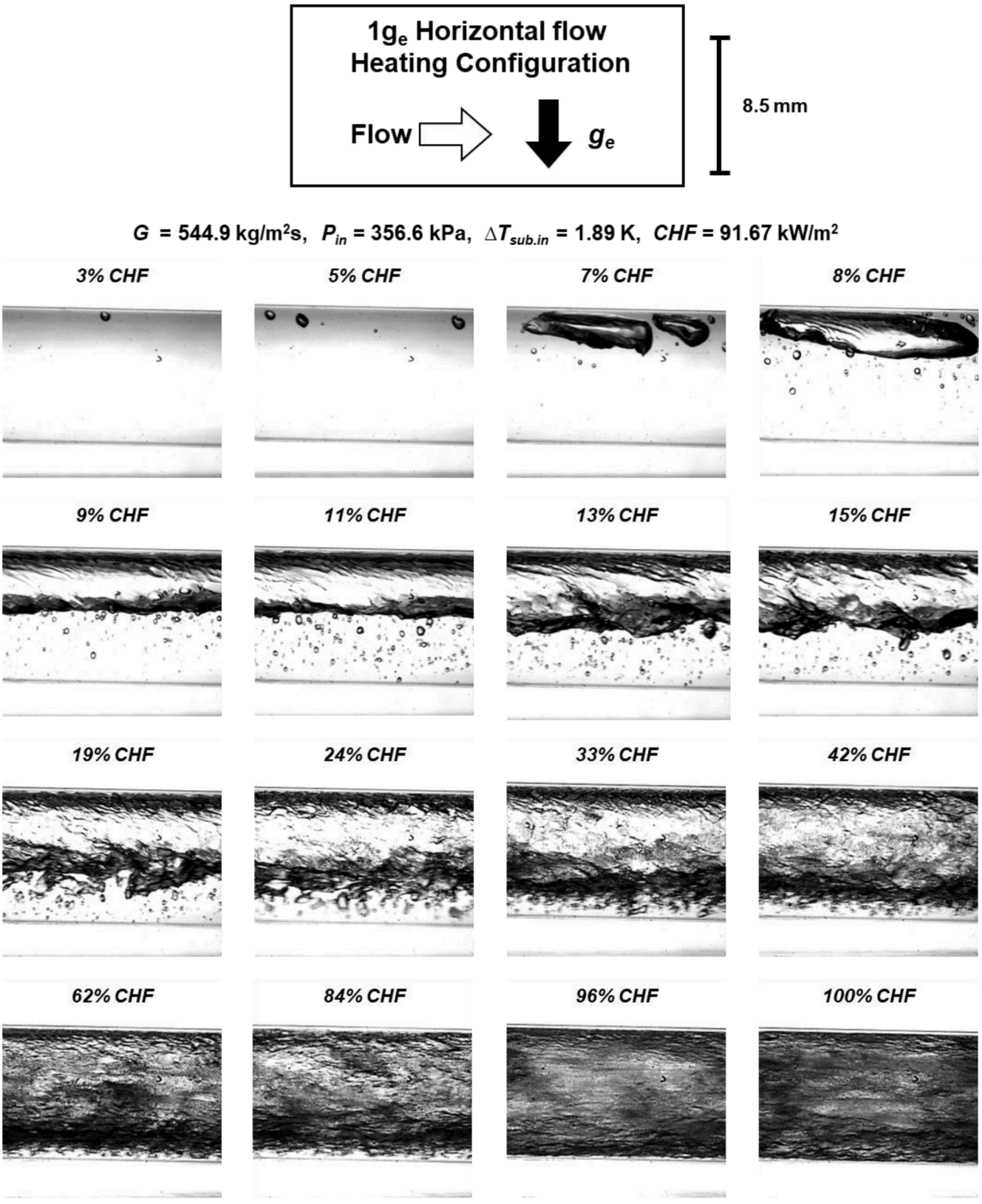


**Fig. 10.** Two-phase flow structure development along the boiling curve for horizontal flow configuration at mass velocity of $G = 544.9$ kg/m$^2$s, inlet pressure of 356.6 kPa, and inlet subcooling of 1.89 K.

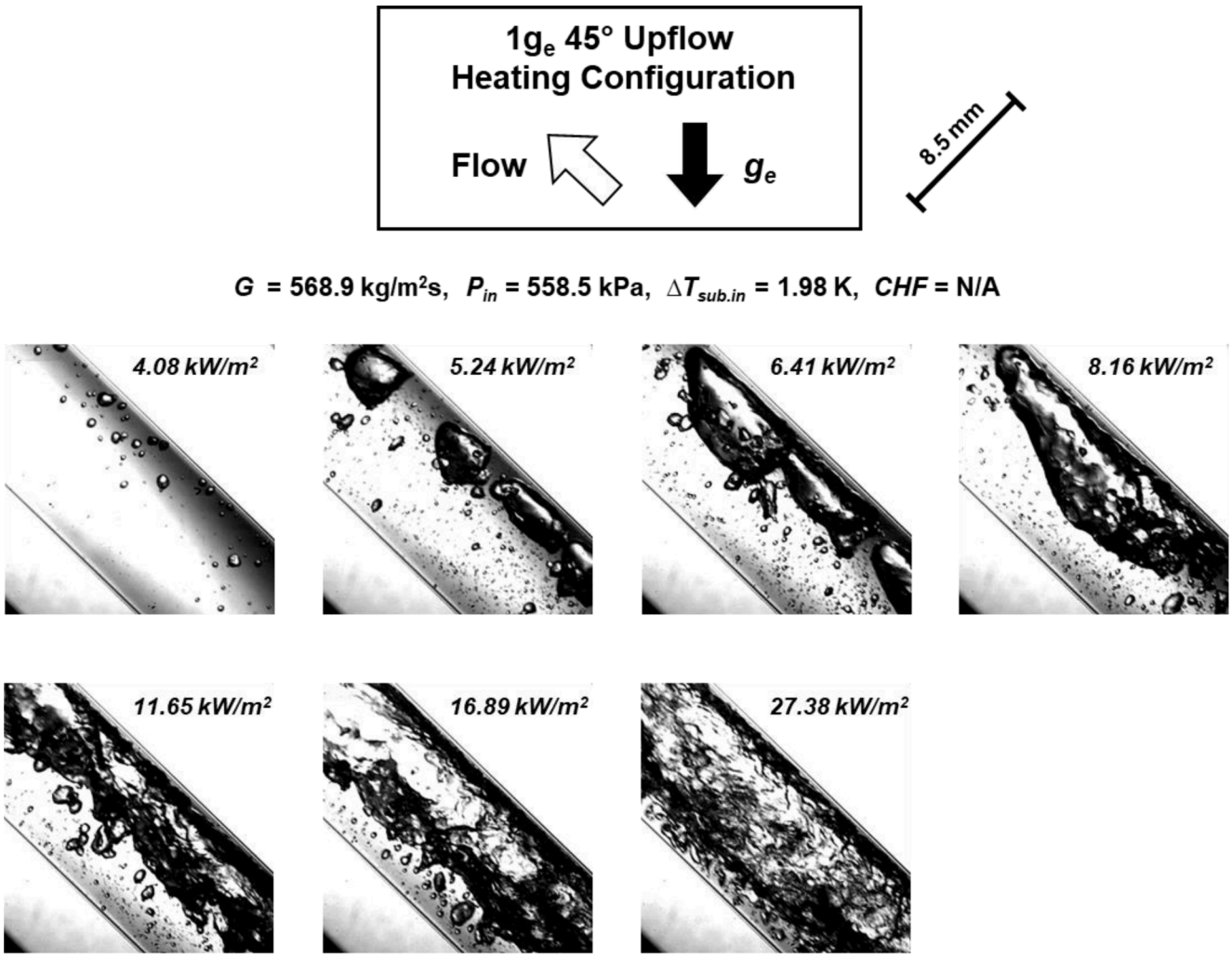


**Fig. 11.** Two-phase flow structure development with increasing heat flux for 45° inclined upflow configuration at mass velocity of $G = 568.9$ kg/m$^2$s, inlet pressure of 558.5 kPa, and inlet subcooling of 1.98 K.

as low as $G = 190$ kg/m$^2$s in the study by Thorncroft et al. [10]. Consequently, at such low velocities, nucleated bubbles were able to slide against the flow direction due to the extremely weak flow inertia and the relatively strong buoyancy force opposing the flow. In contrast, in this study, at $G = 511.1$ kg/m$^2$s, the flow inertia was sufficiently strong to effectively flush bubbles, overcoming the buoyancy force, causing them to slide only in the direction of the flow. With slight increase of heat flux up to 7 % $q''_{CHF}$, a greater number of nucleation sites are activated, intensifying bubble ebullition, and resulted in an increased population of bubbles within visualization tube. Compared to the lower heat flux, noticeably larger center bubbles are observed, which is the result of the agglomeration and coalescence of small bubbles. These large bubbles exhibit an interesting bubble shape resembling *reversed bullet*, with a rounded trailing upper end and a flattened leading lower end. The opposite buoyancy forces acting on the large vapor bubbles in relation to the liquid flow result in their tendency to rise and compete with the inertia of the liquid flow. In the current operating conditions, the vapor bubbles are carried along with the liquid flow. However, at lower mass flow rates, the rising inertia of the bubbles could have potentially surpassed the flow inertia, leading to a backflow phenomenon. From 8 % $q''_{CHF}$ to 13 % $q''_{CHF}$, the observed flow regime is slug. As heat flux increases, the large oblong vapor bubbles are elongated and, at 13 % $q''_{CHF}$, two consecutive oblong bubbles are observed to be in close proximity to each other, nearing the point of merging and forming a single vapor column. When compared to the same heat flux percentage of vertical upflow, the flow in vertical downflow is not as violent, exhibiting a more stable liquid-vapor interface. For instance, at 17 % $q''_{CHF}$ in vertical upflow, liquid-vapor interface experiences significant distortion due to strong turbulence and mixing. In contrast, at 16 % $q''_{CHF}$ in vertical downflow, the interface of the vapor slug appears relatively smoother, with less surface agitation. From 25 % $q''_{CHF}$ to 47 % $q''_{CHF}$, the captured flow patterns are in transition regime between slug and annular flow. Large oblong bubbles are connected, producing a single extended vapor column spanning the entire visualization tube length. Vapor column thickness is not developed enough to occupy the entire cross-section of the tube, leaving abundant space for liquid flow. The vapor column in the flow displays a spiral motion as it descends through the tube, exhibiting lateral wiggling or sideways movement. This spiral motion in vertical downflow was also reported in air-water two phase flow experiments by Oshinowo and Charles [23]. At both 38 % $q''_{CHF}$ and 47 % $q''_{CHF}$, large liquid chunks, indicated with red arrows, are detected within the vapor core. These liquid chunks are assumed to be entrained from annular liquid layer into the vapor core, facilitated by the high shear forces acting on the interface. Once separated from the interface, these liquid chunks "fall", descending downward due to gravity. The entrained liquid fragments play a significant role in cooling down the temperature of the vapor core, maintaining it closer to the saturation temperature and preventing the vapor core from becoming superheated. With a further increase in heat flux, a transition in the flow regime occurs, shifting towards annular flow. For vertical

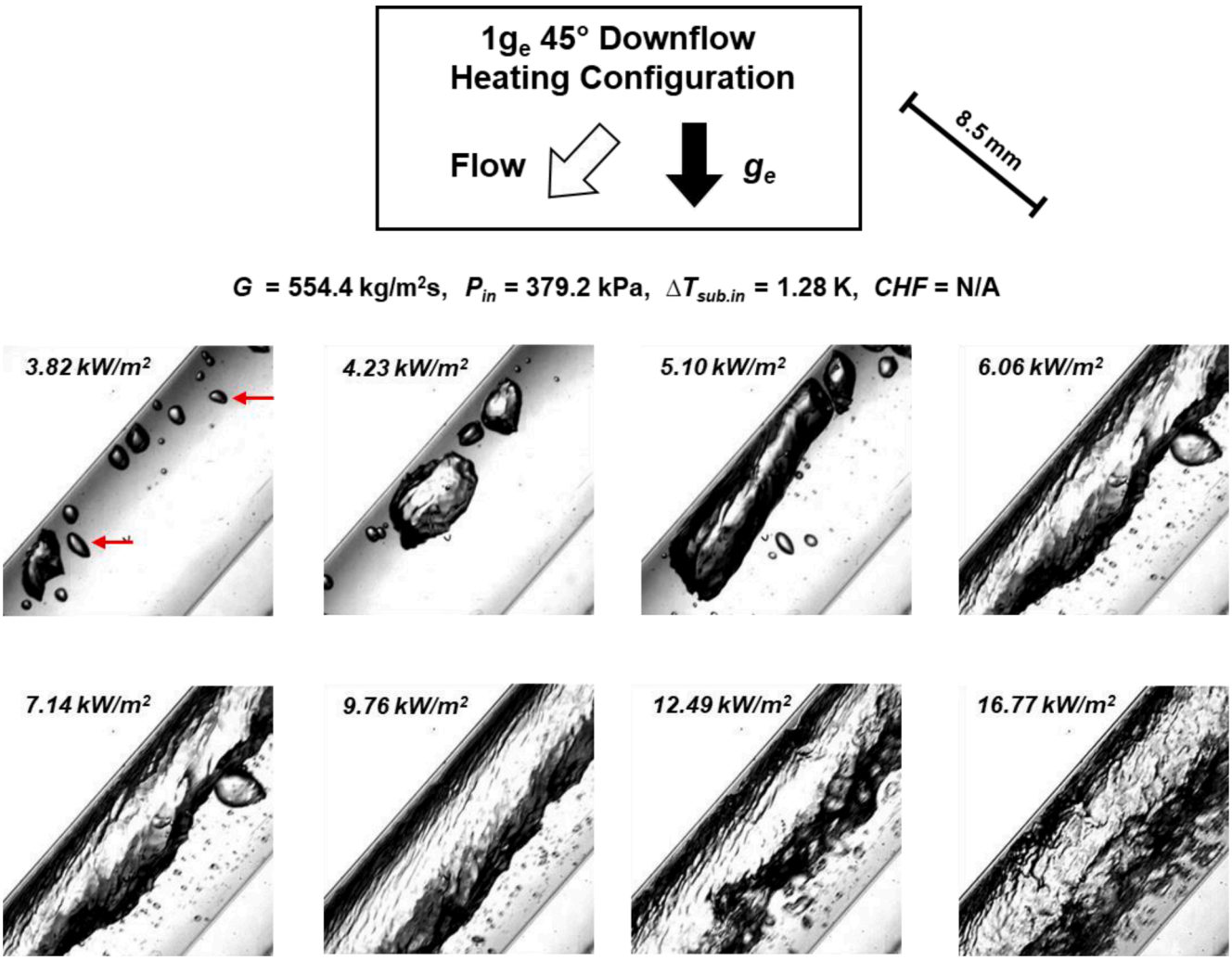


**Fig. 12.** Two-phase flow structure development with increasing heat flux for 45° inclined downflow configuration at mass velocities of $G = 554.4$ kg/m$^2$s, inlet pressure of 379.2 kPa, and inlet subcooling of 1.28 K.

downflow, annular flow is observed starting from 57 % $q''_{CHF}$ up to 100 % $q''_{CHF}$. As the heat flux increases, the vapor core diameter expands, nearly spanning the entire cross-section of the tube, with an extremely thin annular liquid film, especially near the CHF. Similar to vertical upflow, the presence of numerous small bubbles flowing through the annular liquid film suggests active bubble nucleation within the film.

### 3.1.3. *Horizontal flow*

Fig. 10 presents two-phase flow structure and flow patterns captured for $G = 544.9$ kg/m$^2$s, $P_{in} = 356.6$ kPa, $\Delta T_{sub,in} = 1.89$ K in horizontal flow configuration. A single bubble is observed at 3 % $q''_{CHF}$, sliding along the top wall. The recorded bubble wobbles as it slides due to opposite normal vectors acting on the bubble: downward normal force from interfacial shear and upward normal force from buoyancy. Bubbles departed from the bottom surface recondensed back to liquid while traveling across the subcooled liquid core which attributes the absence of bubbles on the bottom wall. At 5 % $q''_{CHF}$, a greater number of nucleation sites are activated and nucleated bubbles are growing into larger size bubbles, yet again, no bubbles are observed at the bottom wall. At 7 % $q''_{CHF}$, large and oblong plug-flow vapor structures are captured alongside discrete tiny bubbles, all of which are concentrated near the top wall region. Further increase of the heat flux leads to more active vapor generation and coalescence resulting in longer and thicker large oblong bubbles, as can be observed at 8 % $q''_{CHF}$. A strong flow orientation effect can be clearly identified from the severe vapor stratification and from the rising small bubbles from beneath. The elongated bubbles expand as they flow by *"sweep and absorb"* process. As it has been predicted by Kim et al. [24], authors of the present study, from their CFD simulations for $LN_2$ flow boiling, large oblong bubbles grow in size not only by interfacial evaporation, but also by actively sweeping and absorbing neighboring bubbles while flowing through a channel. With a gradual increase in heat flux towards 15 % $q''_{CHF}$, the length of oblong bubbles in the flow progressively extends, bringing them closer to each other. Eventually, they merge together, resulting in the formation of continuous vapor over a thick liquid layer. However, note that the flow pattern is not perfect stratified flow having the top surface entirely covered by vapor film. Due to high vapor velocity, liquid flowing under the vapor structure is dragged up and around the periphery, forming a thin layer of liquid fully wetting the tube. This flow pattern is called stratified annular flow as was identified and explained by Van Dresar and Siegwarth [25]. This flow pattern persists until a high heat flux of 84 % $q''_{CHF}$. Similar to both vertical upflow and downflow configurations, it is important to note the presence of numerous bubbles flowing through the liquid beneath the vapor blanket, which can be consistently observed throughout the heat flux range of 9 to 84 % $q''_{CHF}$. The active nucleation and departure of bubbles within the liquid layer contribute to maintaining the bottom wall temperature near the saturation temperature, preventing overheating even under high heat flux conditions. As the heat flux approaches 96 % $q''_{CHF}$, the flow stratification starts to diminish, leading to a transition into annular flow. The

acceleration of the flow, induced by an increasing vapor void fraction, causes the flow inertia to dominate over the effects of gravity. This results in a symmetrical distribution of the liquid film thickness between the top and bottom walls. At the point of CHF, the liquid layer thickness remarkably decreases, particularly near the top surface, which increases the likelihood of partial drying out of the top liquid layer.

#### 3.1.4. 45° inclined upflow

Fig. 11 illustrates two-phase flow structure and flow patterns captured for $G = 568.9$ kg/m$^2$s, $P_{in} = 558.5$ kPa, $\Delta T_{sub,in} = 1.98$ K in 45° upflow configuration. The flow patterns for this orientation resemble those of horizontal flow; bubbly to plug, stratified annular, and finally annular. At 4.08 kW/m$^2$, the tube exhibits dispersed small bubbles, with a discernible concentration towards the upper wall. This spatial distribution can be attributed to the partial gravity effect, which imparts a buoyancy force on the vapor bubbles, causing their preferential ascent towards the upper region of the tube. At 5.24 kW/m$^2$, the observed flow pattern transitions from bubbly to plug. The captured large oblong bubbles exhibit a distinct *"bullet-shaped"* morphology, characterized by a rounded cap head and a flattened tail. Similar plug flow pattern continues to higher heat flux of 8.16 kW/m$^2$, with the oblong bubbles becoming longer and thicker. Further increase in heat flux instigated coalescence of these elongated bubbles resulting in a single continuous vapor blanket, as shown in 11.65 kW/m$^2$. Notice the gradual increase in the number of vapor bubbles within the lower liquid bath and the concurrent enlargement of bubble sizes as the heat flux intensifies. This sequence of events can be elucidated as follows: First, the elevation in heat flux activates a greater number of bubble nucleation sites, resulting in an increased number of nucleating bubbles within the heated test section tube. Second, at elevated heat flux conditions, these nucleated bubbles grow at an accelerated rate and reach their departure diameter faster than they do at lower heat flux conditions. This leads to the release of a larger number of bubbles into the bulk liquid. Consequently, the net effect of the increased heat flux is the augmentation of the bubble population within the lower liquid bath of the flow, as visually captured in the visualization section shown in Fig. 11. In succession, this denser bubble population in the liquid bath encourages interactions, leading to more pronounced bubble coalescence and the eventual formation of larger bubbles. Subsequently, the coalesced large bubbles rise above and are absorbed into the vapor flow, contributing to the expansion of the vapor blanket. At a heat flux of 27.38 kW/m$^2$, the stratified top vapor blanket expands continuously in thickness, occupying a significant portion of the tube diameter. Concurrently, the liquid is displaced towards the outer rim of the tube, forming an annular liquid flow. Furthermore, in line with previous flow orientations, even in the 45° inclined upflow configuration, bubble nucleation persists within the annular liquid film, which can be confirmed by the presence of small bubbles flowing through the thin liquid film.

#### 3.1.5. 45° inclined downflow

Fig. 12 illustrates two-phase flow structure and flow patterns captured for $G = 554.4$ kg/m$^2$s, $P_{in} = 379.2$ kPa, $\Delta T_{sub,in} = 1.28$ K in 45° downflow configuration. The flow patterns for this orientation resemble those of horizontal flow; bubbly to plug, stratified annular, and finally annular. At 3.82 kW/m$^2$ and 4.23 kW/m$^2$, small to large bubbly flow patterns are observed. Similar to 45° upflow orientation, the partial gravity effect induces a normal buoyancy force on the vapor bubbles, which aggregates the vapor structures towards the top wall region of the tube. Similar to vertical downflow configuration, albeit to a lesser extent, a moderate degree of compression can be observed from the skewed bubbles, as indicated with red arrows. This compression is due to the opposite buoyancy force vector against the flow direction, resulting in skewed bubble shapes. Note that the compression was not observed in 45° upflow bubbly flow. With a slight increase in heat flux up to 5.10 kW/m$^2$, a plug flow pattern can be observed. The captured images depict the distinctive shape of the large oblong bubbles, characterized by both ends being flat. In contrast to the previous flow configurations, where the oblong bubbles in plug or slug flow exhibited either a *"bullet shape"* or a *"reverse bullet shape"*, with one edge rounded and the other flat, the large bubble observed in the 45° downflow configuration displays a soft-cornered cuboid shape. From 6.06 kW/m$^2$ to 9.76 kW/m$^2$, the large oblong bubbles in the 45° downflow configuration become elongated and interconnected, forming a continuous vapor blanket that stratifies above the bottom liquid layer. In comparison to a similar flow pattern observed in the 45° upflow image at 11.65 kW/m$^2$ in Fig. 11, the liquid-vapor interface in the 45° downflow configuration is observed to be less wavy. This can be attributed to the relatively smaller phase velocity difference between the vapor blanket and the liquid film in 45° downflow, which is influenced by the additional gravitational draining effect acting on the liquid film. This explanation aligns with the concept of Helmholtz instability theory and highlights the stabilizing effect of smaller phase velocity difference on the liquid-vapor interface. Due to the increasing vapor void fraction, the vapor flow accelerates, resulting in an unstable liquid-vapor interface with chaotic waviness as observed at higher heat flux conditions of 12.49 kW/m$^2$ and 16.77 kW/m$^2$.

#### 3.1.6. Quantification of bubble dynamics

To understand the effect of flow orientation on bubble dynamics, captured flow images from vertical upflow and vertical downflow have further been analyzed. Since the visualization glass tube is not heated and adiabatic, resulted two-phase flow structures from the test section tube can be preserved and visualized in the visualization glass tube. Therefore, the captured interfacial structures can be regarded as a representation of the flow pattern at the end of the heated test section tube. Based on this understanding, various parameters within the visualization glass tube, including the diameter of bubbles attached to the wall, $D_{bw}$, the number of bubbles attached to the wall, $N_{bw}$, the bubble sliding velocity on the wall, $u_{bw}$, and the core velocity, $u_c$, were quantified employing MATLAB software. Note that the measurement error was estimated to be ±1 pixel for the bubble radius, bubble sliding velocity, and core velocity. The measured results are visually represented in Fig. 13 and summarized in Table 3. It should be noted that the current experimental setup is not designed to directly measure and investigate bubble dynamics and nucleation parameters, such as bubble nucleation frequency, bubble growth, bubble departure diameter, and bubble departure frequency, due to the absence of heating in the visualization glass tube. Nevertheless, it is possible to infer the impact of flow orientation on bubble dynamics by analyzing measurable parameters within the visualization glass tube, as presented in Fig. 13.

In Fig. 13(a), the plot illustrates the variation of measured bubble diameter on the wall as a function of heat flux percentage, which is normalized using the measured CHF value at the mentioned operating conditions for each orientations. Several noteworthy trends are discernible within Fig. 13(a). First, for 1-$g_e$ vertical upflow, a pronounced reduction in the size of wall-attached bubbles is evident as the heat flux percentage transitions from 6 % to 8 % $q''_{CHF}$. Second, in contrast, it is challenging to discern clear trends in bubble diameter variation with heat flux for 1-$g_e$ vertical downflow, primarily due to the scattered nature of the measured data. Nonetheless, it is apparent that the measured values exhibit a relatively consistent and comparable value to those observed in 1-$g_e$ vertical upflow, except for the lowest heat flux percentage of 6 % $q''_{CHF}$. Third, irrespective of flow orientation, bubble diameters predominantly fall within the range of 0.2 – 0.4 mm for heat fluxes exceeding 8 % $q''_{CHF}$.

The substantial reduction in bubble diameter observed during the transition from 6 % to 8 % $q''_{CHF}$ in the vertical upflow orientation can be attributed to a significant increase in bubble departure frequency. This phenomenon finds corroboration in the work of Hutter et al. [26], who conducted a single cavity nucleation experiment, wherein they measured bubble departure frequency as a function of wall superheat. They reported a pronounced upsurge in bubble departure frequency at a

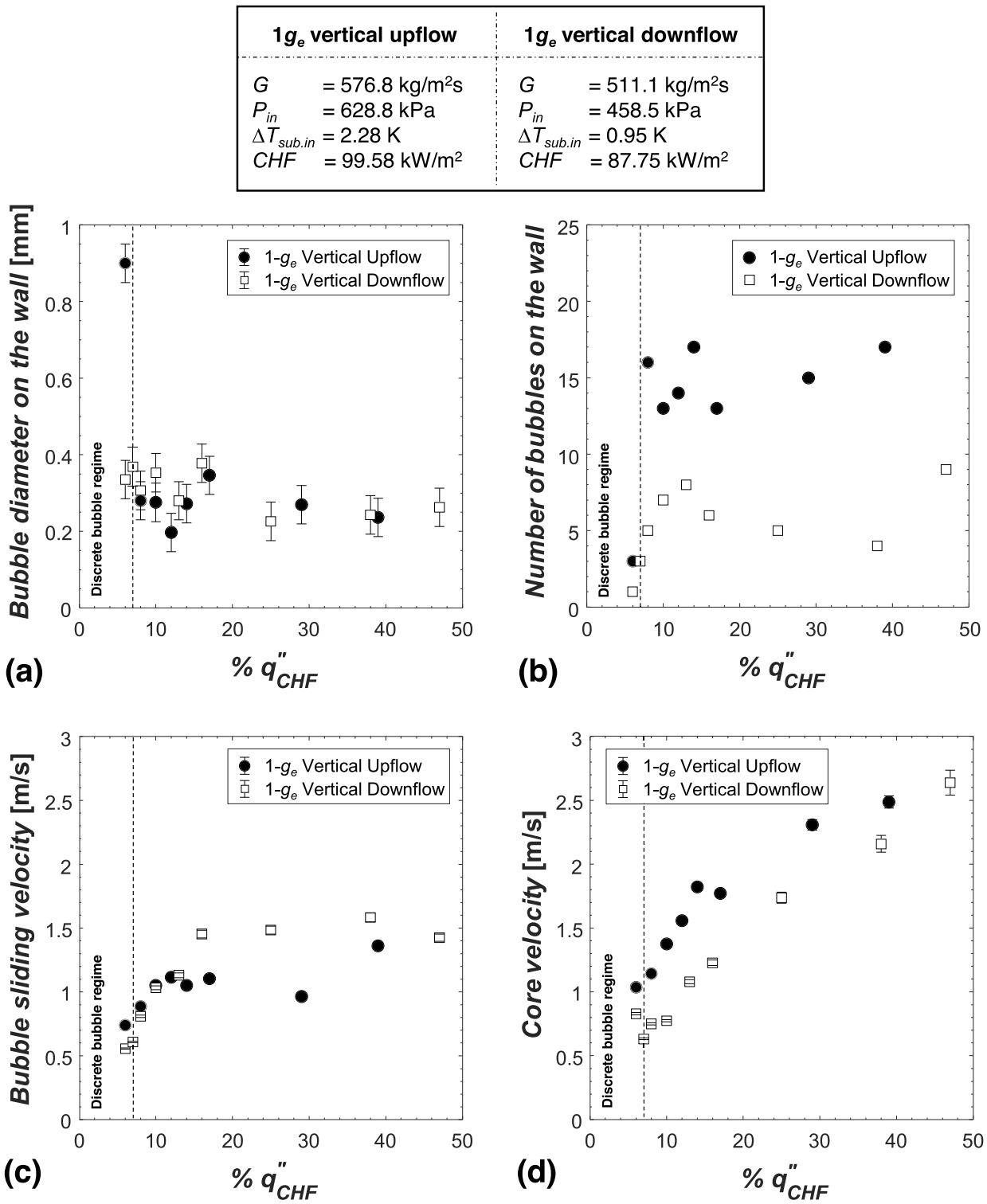


**Fig. 13.** Comparison of variations of (a) bubble diameter on the wall, (b) number of bubbles on the wall, (c) bubble sliding velocity, and (d) core velocity in the downstream adiabatic tube for both vertical upflow and vertical downflow with % CHF.

wall superheat of approximately 3 K, consistently observed across the pressure range of 0.5 – 1.0 bar. Furthermore, they noted a subsequent plateauing trend in bubble departure frequency following the initial surge. The trend in bubble departure frequency reported by Hutter et al. [26] can be linked to the findings of the current experiment by considering the relationship between bubble departure diameter and bubble departure frequency, as reported by Zuber [27],

$$fD_b = C\left[\frac{\sigma g(\rho_f - \rho_g)}{\rho_g^2}\right] \tag{10}$$

As indicated by the functional relationship, the bubble departure diameter and bubble departure frequency exhibit an inverse proportionality. Consequently, drawing upon the insight provided by Zuber, the abrupt decrease in the measured bubble diameter during the

**Table 3**
Bubble dynamics parameters measured in the downstream a diabatic tube for vertical upflow and vertical downflow for different values of % CHF.

| *Vertical Upflow* | | | | |
|---|---|---|---|---|
| $\%q''_{CHF}$ [%] | $D_{bw}$ [mm] | $N_{bw}$ [-] | $u_{bw}$ [m/s] | $u_c$ [m/s] |
| 6 | 0.900 | 3 | 0.74 | 1.04 |
| 8 | 0.280 | 16 | 0.89 | 1.14 |
| 10 | 0.276 | 13 | 1.05 | 1.38 |
| 12 | 0.197 | 14 | 1.11 | 1.56 |
| 14 | 0.273 | 17 | 1.05 | 1.82 |
| 17 | 0.346 | 13 | 1.11 | 1.77 |
| 29 | 0.270 | 15 | 0.97 | 2.31 |
| 39 | 0.237 | 17 | 1.36 | 2.49 |
| *Vertical Downflow* | | | | |
| $\%q''_{CHF}$ [%] | $D_{bw}$ [mm] | $N_{bw}$ [-] | $u_{bw}$ [m/s] | $u_c$ [m/s] |
| 6 | 0.335 | 1 | 0.56 | 0.83 |
| 7 | 0.369 | 3 | 0.61 | 0.63 |
| 8 | 0.307 | 5 | 0.81 | 0.75 |
| 10 | 0.353 | 7 | 1.03 | 0.77 |
| 13 | 0.280 | 8 | 1.13 | 1.08 |
| 16 | 0.378 | 6 | 1.45 | 1.23 |
| 25 | 0.226 | 5 | 1.48 | 1.74 |
| 38 | 0.243 | 4 | 1.58 | 2.16 |
| 47 | 0.263 | 9 | 1.42 | 2.64 |

transition from 6 % to 8 % $q''_{CHF}$ can be attributed to a sudden increase in bubble departure frequency, which occurs as the wall superheat increases in response to the elevated heat flux percentage, as reported in Hutter et al. [26].

Under the lowest heat flux condition (6 % $q''_{CHF}$), the measured bubble diameter is 0.335 mm for vertical downflow, while it reaches 0.9 mm for vertical upflow. The smaller bubble diameter in vertical downflow compared to vertical upflow can be attributed to the difference in the duration bubbles remain attached to the heated wall. In vertical downflow, the opposing direction of buoyancy and flow leads to an additional lifting force on bubbles, causing earlier detachment from the wall. Consequently, bubbles in vertical downflow cannot grow larger and are detached as smaller bubbles. In contrast, in vertical upflow, where the buoyancy vector aligns with the flow direction, bubbles remain attached to the heated wall and tend to slide along the heated wall, increasing the time for further growth before detachment. This observation suggests an inference that the bubble frequency for vertical downflow exceeds that for vertical upflow. To further validate the impact of flow orientation on bubble departure frequency, the population of wall-attached bubbles was quantified and illustrated as a function of heat flux percentage, as shown in Fig. 13(b). The number of bubbles attached to and sliding along the wall is significantly higher in vertical upflow compared to vertical downflow across the entire range of logged heat flux percentages. This clearly indicates more frequent bubble lift-off events in vertical downflow, leading to fewer bubbles remaining on the tube wall. As previously discussed in Sections 3.1.1 and 3.1.2, Thorncroft et al. [10] linked the extended periods of bubble sliding and dwelling on the heated wall in vertical upflow configurations to enhanced heat transfer performance. They posited that this phenomenon contributes to heightened heat transfer efficiency in vertical upflow as compared to vertical downflow configurations. This trend well aligns with the heat transfer performance trends observed in this experimental results, as will be exhibited in the later Section 4.2.

In Fig. 13(c) and Fig. 13(d), the plots illustrate the variation of measured bubble sliding velocity and core velocity as a function of heat flux percentage, respectively. Several noteworthy trends are discernible within the figures. First, as illustrated in Fig. 13(c), the bubble sliding velocity exhibits a common pattern for both flow orientations, with an initial increase in velocity that eventually levels off as heat flux increases. Second, the curve representing bubble sliding velocity for vertical downflow intersects and surpasses the curve for vertical upflow, ultimately reaching a higher sliding velocity under high heat flux conditions. Third, core velocities in both flow orientations demonstrates a consistent pattern characterized by almost linearly increasing velocity as heat flux levels increase. This increasing core velocity can be attributed to flow acceleration induced by the escalating void fraction corresponding to the increased heat flux. Fourth, despite the common linearly increasing trend, the core velocity in vertical upflow consistently maintains a higher magnitude compared to the core velocity observed in vertical downflow. The consistently higher core velocity for vertical upflow is a direct consequence of buoyancy force accelerating the flow especially at higher heat flux conditions where vapor void fraction is primarily concentrated at the core, such as annular flow. In contrast, in vertical downflow, within a similar flow structure of annular flow, buoyancy force acts as a resisting force on the vapor core, opposing the flow direction and contributing to a reduction in the core velocity.

Overall, the analysis of the quantified parameters extracted from the recorded flow images has facilitated an examination of the influence of flow orientation on bubble size, bubble population, bubble sliding velocity, and core velocity. Nevertheless, it is important to note that the current experimental facility is not tailored for conducting in-depth investigations into bubble dynamics. Consequently, future experiments should be conducted with a more comprehensive approach, with particular emphasis on the following aspects:

(a) Visualizing the heated length specifically tailored for cryogenic flow boiling.
(b) Directly measuring bubble departure frequency and bubble departure diameter for cryogenic flow boiling.
(c) Developing empirical correlations for bubble nucleation, bubble growth, and bubble departure frequency tailored for cryogenic flow boiling.

### 3.1.7. Bubble collision dispersion phenomenon

Upon careful investigation of the recorded flow images, an interesting bubble dynamic behavior known as *bubble collision dispersion* is observed in various flow orientations. Fig. 14(a) illustrates bubble collision dispersion process captured at $G = 576.8$ kg/m$^2$s, $P_{in} = 628.8$ kPa, $\Delta T_{sub,in} = 2.28$ K, and $q'' = 7.97$ kW/m$^2$ in vertical upflow configuration. Flow images are captured with a time step of 0.7 ms at steady state. At the initial time frame of $t_0$, the red box highlights three neighboring small bubbles that are the subject of interest. Among these bubbles, the two uppermost are attached to the wall, while the third is flowing underneath them. As the flow progresses, the bottommost bubble accelerates and approaches the other two until $t_0 + 2.8$ ms, at which point the bubbles are tightly packed together, appearing squeezed. At $t_0 + 3.5$ ms, all three bubbles are observed to be in contact with each other, indicating the moment of collision. After the collision, from $t_0 + 3.5$ ms to $t_0 + 4.2$ ms, the top and bottom bubbles bounce off in opposite directions, instead of merging. The described bubble behavior resembles the movement of three rigid bodies, bouncing away from each other after a head-to-head collision. The collision between the bubbles generates repelling momentum, leading to a dispersion force that caused the bubbles to bounce off each other and scatter. This dispersion process is evident from $t_0 + 4.9$ ms to $t_0 + 6.4$ ms, as the distances between the three bubbles progressively increase with time, indicating that the collided bubbles are scattering away from each other.

Fig. 14(b) presents bubble collision dispersion process captured at $G = 544.9$ kg/m$^2$s, $P_{in} = 356.6$ kPa, $\Delta T_{sub,in} = 1.89$ K, and $q'' = 10.08$ kW/m$^2$ in horizontal flow configuration. Flow images are captured with a time step of 1.4 ms at steady state. The sequence of flow images captures a series of collisions and dispersions. At the initial time frame of $t_0$, the red box highlights a large bubble and a group of smaller bubbles, all of which are the focus of attention. Over time, the large bubble approaches the smaller bubbles, leading to their close proximity at $t_0 + 1.4$ ms. From $t_0 + 1.4$ ms to $t_0 + 2.8$ ms, the bubbles are squeezed and tightly packed

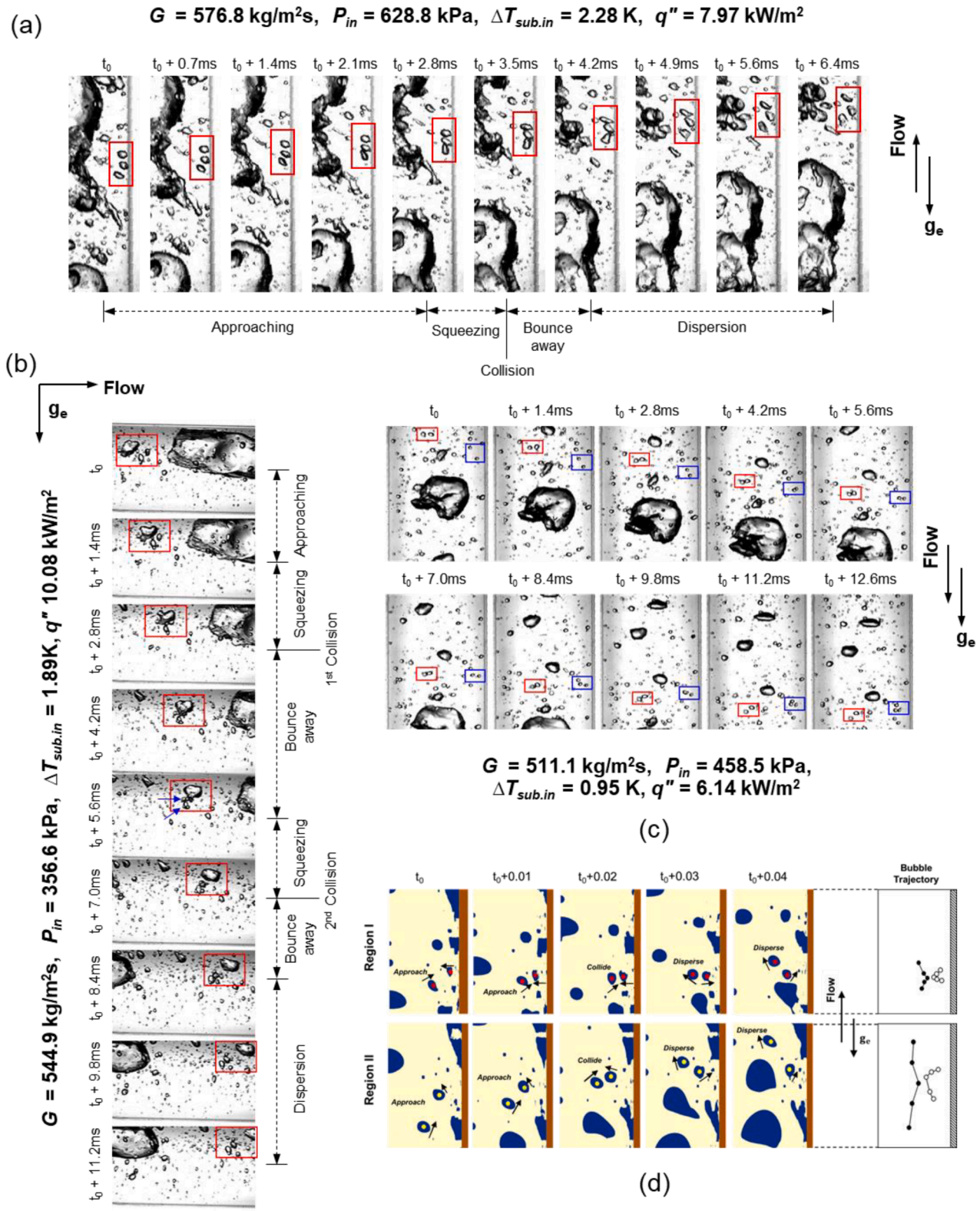


**Fig. 14.** Experimentally captured bubble collision dispersion dynamics in (a) vertical upflow, (b) horizontal flow, and (c) vertical downflow, along with (d) CFD simulated bubble collision dispersion from Kim et al. [24].

together. At $t_0 + 2.8$ ms, the first collision occurs among the bubbles in the cluster. Following the collision, from $t_0 + 2.8$ ms to $t_0 + 5.6$ ms, the collided small bubbles disperse away from the large bubble, increasing their distance from it. Notice the relatively minor impact of the collision on the trajectory of the large bubble compared to those of smaller bubbles. The difference can be attributed to the larger size of the bubble which requires larger momentum to alter its pathway. As a serial event, the dispersed small bubbles initiate another set of collision and dispersion. At $t_0 + 5.6$ ms, two small bubbles, previously repelled from the first collision, approach the remaining small bubbles as indicated by the blue

arrows. As they get closer in proximity, the group of bubbles is compressed, forming a tightly packed cluster, leading to the second collision at $t_0$ + 7.0 ms. Following the second collision, the bubbles exhibit a uniform bouncing behavior, suggesting a more symmetrical dispersion pattern. This behavior is attributed to the similar sizes of the bubbles involved in the collision event. The captured flow image at $t_0$ + 8.4 ms confirms the uniform bouncing of the bubbles, which is followed by continuous dispersion of the bubbles as illustrated from $t_0$ + 8.4 ms to $t_0$ + 11.2 ms.

Similar bubble collision and dispersion dynamics are captured in vertical downflow configuration as presented in Fig. 14(c) at $G = 511.1$ kg/m$^2$s, $P_{in} = 458.5$ kPa, $\Delta T_{sub,in} = 0.95$ K and $q'' = 6.14$ kW/m$^2$. Here, two simultaneous collision and dispersion events are captured, indicated with red and blue boxes over the recorded time period. Likewise, the bubble collision and dispersion behaviors are prevalently observed throughout the $LN_2$ flow boiling of various flow orientations.

Until very recently, the observed bubble collision and dispersion phenomena were not identified or adequately modeled for inclusion in flow boiling CFD. Using existing interfacial models, predictions of phase distribution consistently fell short in terms of accuracy when assessed against measured void fraction distributions [28]. The inaccuracy of these existing interfacial models arises from their reliance on the behavior of single, isolated bubbles which is then extrapolated to dispersed two-phase flow, with the assumption that the overall behavior of the bulk bubbly flow mirrors the behavior of individual bubble. However, as observed from Fig. 14, it is obvious that a bubble in a liquid phase frequently collide with neighboring bubbles without substantial coalescence, leading to alterations in vapor distribution across and along the flow channel. Moreover, it is essential to note that the accuracy of predicting void fraction is paramount in flow boiling system, as it forms the critical foundation for accurate estimations of various two-phase heat transfer parameters, including wall temperature, fluid temperature, and HTCs. Therefore, in order to enhance the predictive accuracy of the flow boiling CFD, Sharma et al. [28] developed a phenomenological model that captures several critical trends in the observed phenomena: (a) the rate of these collisions depends upon the bubble approach velocity and bubble spacing, (b) the bubble collision frequency is expected to be higher in locations with higher bubble concentrations, i.e., larger vapor volume fraction, and (c) the random collision causes the diffusion of the bubbles from high concentration to low concentration, as demonstrated as,

$$F^{BCD} = -\left(K\frac{\rho_f u_t^2}{2\alpha_{max}^{2/3}}\right) f(\alpha)\nabla\alpha \tag{11}$$

where $\alpha_{\max}$ and $K$ are *dense packing limit* and proportionality constant, with recommended values for bubbly flow of 0.62 and 1, respectively, and $\alpha$ is void fraction. Also included in Eq. (11) are liquid fluctuation velocity, $u_t$, resulting from liquid agitation, which accounts for turbulent intensity effects on bubble dispersion, and function $f(\alpha)$, defined as

$$f(\alpha) = \alpha_g^{2/3}\left[1 - \left(\frac{\alpha_g}{\alpha_{max}}\right)\right] \tag{12}$$

Sharma et al. [28] explained that strong bubble diffusion happens as a consequence of the dense packing of bubbles, leading to increased collision frequencies among neighboring bubbles. As a result of random collisions without significant coalescence, bubbles are repelled from higher concentration to lower concentration as there are more collisions in the higher concentration region. Consequently, the net collision force is expected to act in the opposite direction and be proportional to the gradient of void fraction, $\alpha_g$. This explanation aligns well with the phenomena observed in Fig. 14, where the identified process of "approach - squeeze - collision - bounce off - disperse" accurately represents the repelling nature of the bubble collision dispersion force as the distance between bubbles decreases. Kim et al. [24], employed the aforementioned model in their computational simulation of cryogenic flow boiling in a vertical upflow configuration. The simulated bubble collision and dispersion behavior, corresponding to the adopted model, is illustrated in Fig. 14(d). The predicted flow sequence accurately captures the bubble approaching – colliding – dispersing processes occurring in two distinct regions within the flow domain, closely mimicking the observed physical bubble behaviors captured in Fig. 14 (a) to (c). They noted that when the bubble collision dispersion force was excluded from their CFD model, the corresponding error in predicted void fraction experienced a substantial increase compared to the results obtained with the inclusion of the bubble collision dispersion force. Sharma et al. [28] also reported improved accuracy in the lateral phase distribution prediction when incorporating the bubble collision dispersion force into their two-phase flow boiling CFD model. Overall, the experimentally observed bubble collision dispersion phenomena serve as compelling evidence of the existence of this force, which highlights the potential necessity to consider the effect of the force in computational models when simulating momentum exchange in flow boiling scenarios.

## 4. Heat transfer results and discussion

### 4.1. Flow boiling curves

The boiling curves for the five distinct flow orientations are depicted in Figs. 15 to 17, corresponding to streamwise locations of $z = 245$ mm and $z = 505$ mm relative to the inlet of the heated test section, which are representative of the upstream and downstream regions, respectively. The specific operating conditions for each boiling curve are provided within the figures. By examining the local boiling curves for all orientations, notable patterns can be observed, suggesting common trends across the dataset. In the initial phase of the boiling curve, wall temperature linearly increases due to the dominant influence of single-phase liquid convection, reflected by nearly constant slope of the curve. As bubble nucleation commences, there is a remarkable increase in the slope of the boiling curve, reflecting large increases in heat flux corresponding to relatively moderate increases in the wall superheat. This indicates the transition to nucleate boiling, where heat transfer is effectively facilitated by the formation and detachment of bubbles, fostering efficient cooling of the heated wall. Upon further increase in the heat flux, the boiling curves begin to deviate from the nucleate boiling regime and the heat transfer efficiency degrades, which are represented as higher increasing rate of wall superheat and degrading slope of the curves. This transition point is commonly referred to as the Onset of Nucleate Boiling Departure (ONBD). In the final portion of the presented boiling curves, the slope of the curves progressively decreases. Here, large portions of the wall experience intermittent or partial dryout by large coalesced vapor structures, resulting in reduced availability of liquid at the wall for further boiling. Due to the exposure to a vapor-only environment, where heat transfer is predominantly governed by single phase vapor convection, an unsteady rise in wall temperature ensues, eventually reaching the CHF point. Based on the identified common trends, the distinct behaviors of the boiling curves for each flow orientation are carefully investigated.

Fig. 15 shows the boiling curves for vertical upflow and downflow at streamwise locations of $z = 245$ and 505 mm with respect to the inlet of the heated test section. Note that the displayed boiling curves were generated using circumferentially averaged wall temperatures (left wall and right wall) at each axial location to ensure a comprehensive representation of the thermal behavior within the circular channel in vertical configurations. In each boiling curve, a dotted line has been included to indicate the linear tangent of the boiling curves, highlighting the range of nucleate boiling dominant regime. The lower point of intersection represents transition from single phase liquid convection dominant regime to nucleate boiling dominant regime, while the upper point of transition represents ONBD. In both vertical upflow and downflow, the slope of the tangent line is observed to be steeper at the

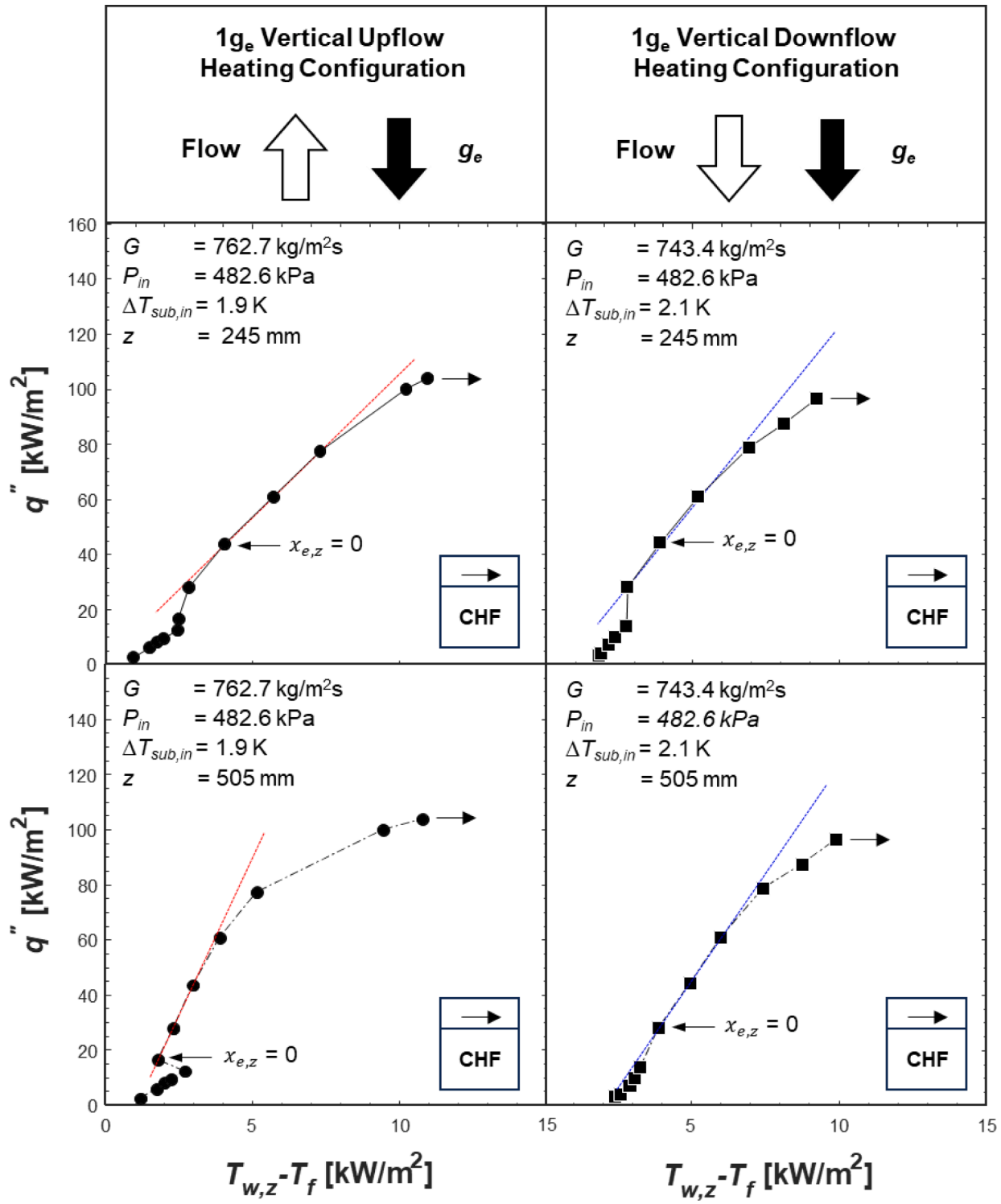


**Fig. 15.** Local boiling curves for vertical upflow and downflow at upstream ($z = 245$ mm) and downstream ($z = 505$ mm) locations for similar operating conditions.

downstream location ($z = 505$ mm) compared to the upstream location ($z = 245$ mm). However, it is interesting to note that the difference in slope is more pronounced in vertical upflow boiling, showcasing the impact of flow orientation on the boiling characteristics and heat transfer performance. Furthermore, it is observed that the transition into and out of the nucleate boiling dominant regime in vertical upflow requires higher heat fluxes at the upstream location compared to those at the downstream location. However, in the vertical downflow configuration, it is observed that the transitions into and out of the nucleate boiling dominant regime occur under similar heat fluxes at each axial location.

Fig. 16 presents the boiling curves for horizontal flow at streamwise locations of $z = 245$, and 505 mm from inlet of the test sections. For horizontal flow, separate boiling curves are generated for both top and bottom walls. In each boiling curve, a dotted line is added to indicate the linear tangent of the boiling curves, representing nucleate boiling dominant regime. During single phase liquid convection regime, the slope of the boiling curve remains nearly constant for both top and

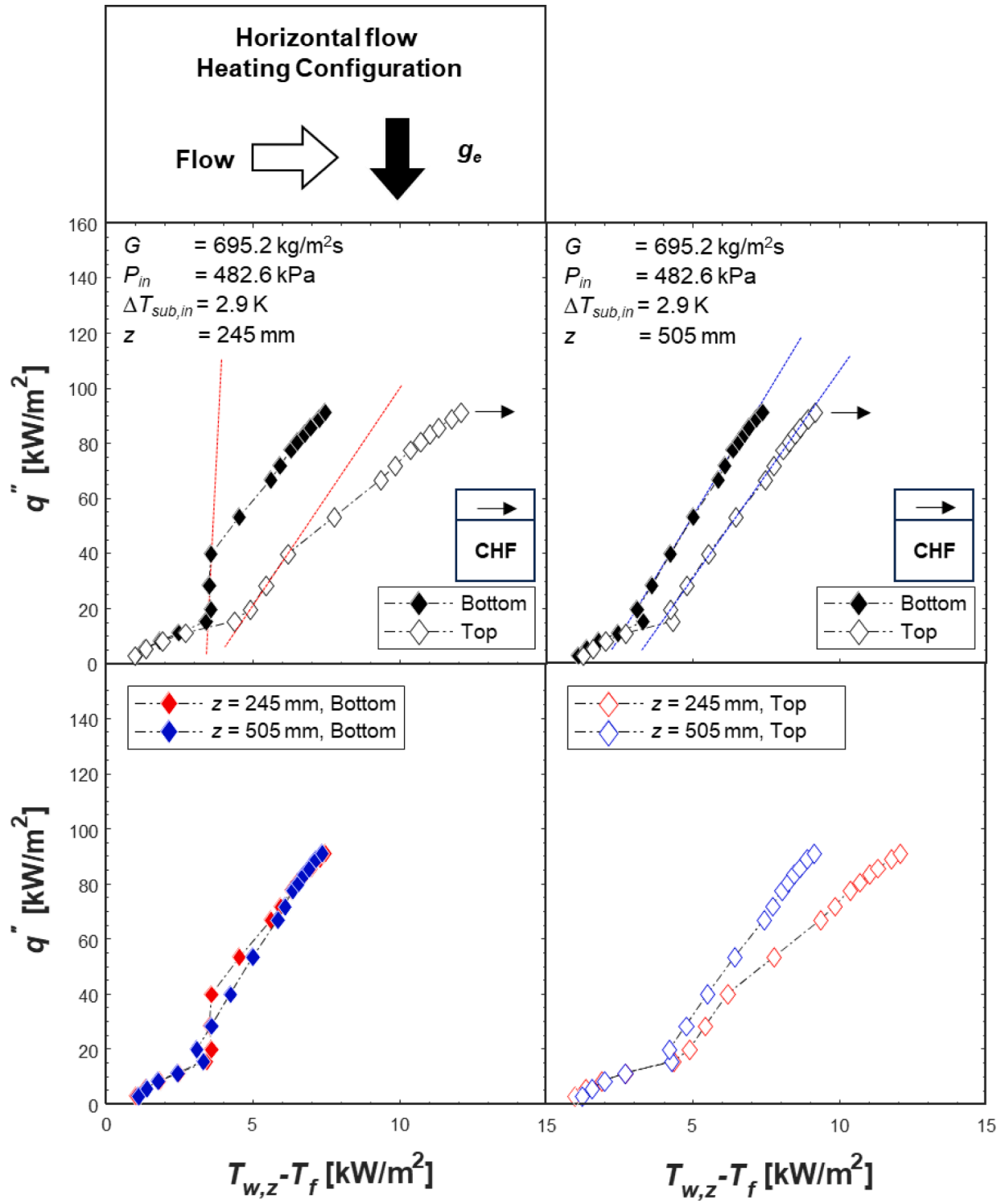


**Fig. 16.** Local boiling curves for horizontal bottom and top walls at upstream ($z$ = 245 mm) and downstream ($z$ = 505 mm) locations, and their comparisons at mass velocity of 695.2 kg/m$^2$s, inlet pressure of 482.6 kPa, and inlet subcooling of 2.9 K.

bottom wall showing minimal circumferential temperature difference. However, as the flow transitions into nucleate boiling dominant regime, the top wall temperature begins to rise higher than the bottom wall temperature, reflecting the presence of asymmetrical flow patterns. As was confirmed in flow visualizations in Fig. 10, asymmetrical flow patterns emerge as early as 9 % $q''_{CHF}$ in horizontal flow orientation, leading to circumferential variation in wall temperature. Noticeably, at upstream location of $z$ = 245 mm, the effect of asymmetrical flow patterns is evident from the difference in slope between the linear tangents for the top and bottom walls. The slope is steeper for the bottom wall compared to the top wall. In contrast, at downstream location of $z$ = 505 mm, the slope difference is minimal due to a decreased slope for the bottom wall relative to the upstream location. By comparing the boiling curves of the same bottom wall but for different axial locations, it is clear that the curves overlap each other in the higher heat flux region. As the heat flux increases, the slope of the upstream boiling curve

deteriorates, but it can be observed that this degradation is limited to the slope of the downstream boiling curve.

Fig. 17 exhibits the boiling curves for 45° inclined upflow and downflow at streamwise locations of $z = 245$, and 505 mm from inlet of the heated test section. For 45° inclined flow, the displayed boiling curves are generated using the bottom wall temperatures at each axial location. Here, regardless of the orientation and axial location, the slopes of the linear tangents are similar to each other, indicating comparable heat transfer efficiency at both orientations. The only notable distinction between 45° upflow and downflow configurations is the larger deviation from nucleate boiling after the ONBD transition in 45° inclined downflow. The increased deviation can be attributed to a greater accumulation of vapor caused by the buoyancy force effect in the 45° downflow configuration.

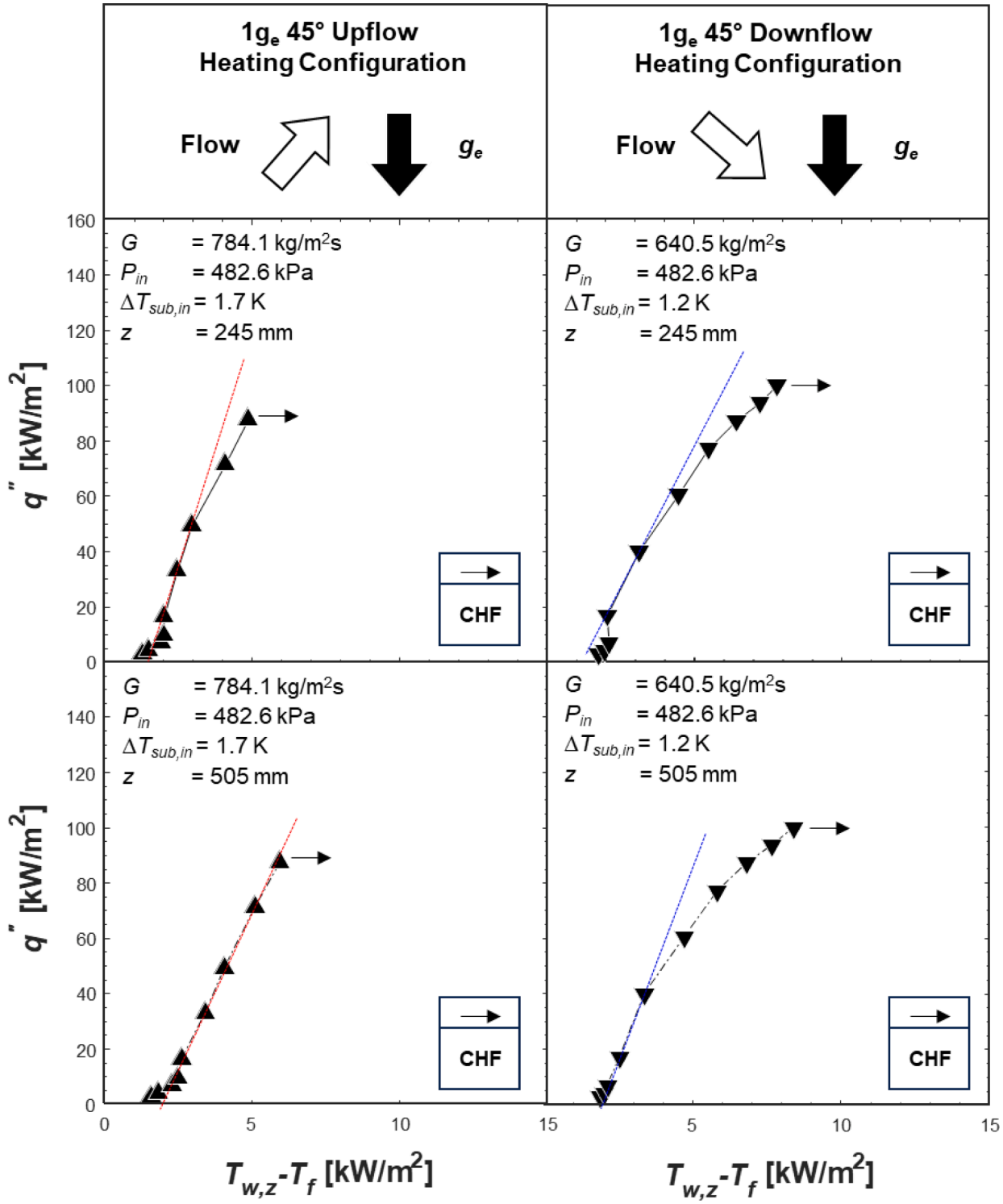


**Fig. 17.** Local boiling curves for 45° inclined upflow bottom wall and 45° inclined downflow bottom wall at upstream ($z = 245$ mm) and downstream ($z = 505$ mm) locations for similar operating conditions.

### 4.2. Flow orientation effects on heat transfer coefficient

The effect of body force on flow boiling can be analyzed using two different approaches. First, parabolic flight experiments can be conducted to simulate a microgravity environment and explore the reduced gravity effect on flow boiling performance. Second, under Earth gravity, flow orientation can be rotated to vary the effective normal gravitational acceleration and examine its impact on flow boiling system. Previous research by Kim et al. [17] investigated microgravity flow boiling and analyzed the corresponding heat transfer results obtained from cryogenic flow boiling experiments during parabolic flights. The present study investigates the effect of body force on cryogenic flow boiling by rotating the flow orientation from vertical upflow ($\theta = 90°$) to vertical downflow ($\theta = 270°$) with angular variation of 45°

In Fig. 18, variation of averaged heat transfer coefficient with increasing wall heat flux is presented for different flow orientations under Earth gravity, in addition to the results obtained from the microgravity experiments by Kim et al. [17]. The operating conditions for the cases encompass a mass velocity range of $G = 664.3 \pm 21.6$ kg/m$^2$s, inlet pressure of $P_{in} = 482.6$ kPa, and an inlet subcooling range of $\Delta T_{sub,in} = 1.6 \pm 0.5$ K. The mass velocity differences among the cases are within ±3 %, which is narrow enough to neglect the effect of mass velocity. Note that for horizontal flow, 45° inclined upflow, and 45° inclined downflow, the heat transfer coefficients for the bottom wall are utilized to construct the figure. The presented heat transfer coefficient curves commonly exhibit a sharp and almost linearly increasing trend with increasing heat flux at the lower heat flux range. Subsequently, the slope of the curves progressively decreases, displaying comparatively moderate changes in heat transfer coefficients until CHF. The strong correlation between the heat transfer coefficients and the wall heat flux at the lower heat flux range suggests that the dominant heat transfer mechanism in this regime is nucleate boiling. The gradually decreasing slope of the heat transfer coefficient curve is a result of a well-known flow boiling phenomenon called suppression of nucleate boiling. This suppression effect can be expressed with a simple functional description of nucleate boiling heat transfer coefficient as

$$h_{nb} = S \cdot h_{pb} \; where \begin{cases} h_{pb} = f(q'') \\ S = f(G,\ x_e) \end{cases} \tag{13}$$

wherein the nucleate boiling heat transfer coefficient, $h_{nb}$, is expressed as the product of the pool boiling heat transfer coefficient, $h_{pb}$, and 'suppression factor', $S$. $h_{pb}$, as widely observed from numerous pool boiling experiments, exhibits well-established correlation with the heat flux $q''$, which arises from the effect of bubble nucleation, an increased number of active nucleation sites, and intensified bubble growth rate and departure frequency. The suppression factor, $S$, which can be expressed as a function of mass velocity, $G$, and equilibrium quality, $x_e$, corrects the fully developed nucleate boiling prediction from $h_{pb}$ to account for the fact that in flow boiling: (a) as the flow inertia effect increases in strength, nucleation is more strongly suppressed; and (b) as flow quality increases, convective evaporation at the interface overpowers nucleate boiling and further suppresses bubble nucleation. Based on the functional form, the decreasing slope of the $h_{tp,avg}$ curve can be

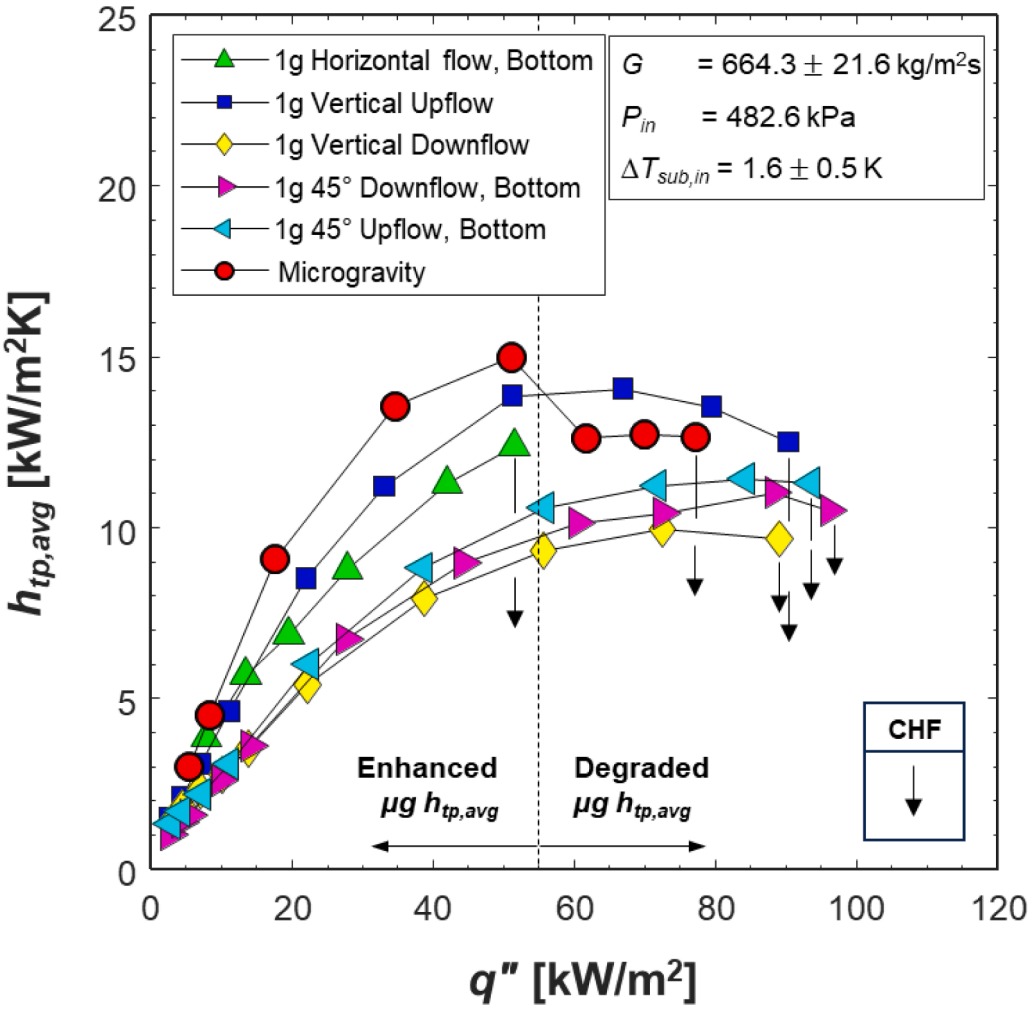


**Fig. 18.** Variation of average heat transfer coefficient with heat flux for five different flow orientations in 1-$g_e$ and microgravity under similar operating conditions.

attributed to the intensifying suppression of nucleate boiling, which is primarily driven by the increasing flow quality resulting from the escalating heat flux. Lastly, the moderate changes in heat transfer coefficients observed at higher heat fluxes are indicative of the characteristic behavior of cryogenic flow boiling, which can be attributed to the continuous presence of nucleate boiling within the annular liquid layer, without being fully suppressed. This trend is supported by comprehensive flow visualizations collected across all the flow orientations, as presented Figs. 8–12. The captured flow images reveal the presence of numerous small bubbles flowing through the annular liquid layer, providing clear evidence of the sustained nucleate boiling at high heat fluxes. This persistence of nucleate boiling contributes to the preservation of a high heat transfer coefficient without experiencing significant deterioration at high heat flux conditions, at least until CHF.

While sharing the described similar trends, a distinct hierarchy of average heat transfer coefficients is evident among the different cases. Under Earth gravity (1-$g_e$), vertical upflow exhibits the highest heat transfer coefficient across the entire heat flux range. Following vertical upflow, horizontal flow ranks as the second highest. However, in horizontal flow, the heat transfer coefficient curve is restricted to a lower range of heat flux due to partial dryout at the top wall, resulting in a lower CHF compared to other orientations. For 45° inclined upflow and downflow, average heat transfer coefficient curves almost overlap each other, presenting minor difference between the two orientations, while both orientations yield lower heat transfer coefficients in comparison to horizontal flow. Lastly, vertical downflow demonstrates the lowest average heat transfer coefficients for the entire heat flux range, albeit a small difference with the 45° inclined orientations. The superior heat transfer efficiency in vertical upflow can be attributed to the effect of buoyancy force, which is aligned with the flow direction. The buoyancy force in vertical upflow facilitates the removal of vapor structures from the heated section, allowing for sufficient liquid replenishment and effective wall temperature cooling. Furthermore, as visually confirmed in Fig. 8, and supported by the findings of Thorncroft et al. [10], bubble sliding is prominent in vertical upflow. The enhanced bubble sliding contributes to an improved heat transfer efficiency by prolonging the duration of latent heat transfer. In contrast, vertical downflow shows the lowest heat transfer efficiency as a result of the counteracting buoyancy force that leads to the accumulation of vapor structures within the heated section, consequently hindering effective liquid replenishment. Moreover, as reported by Thorncroft et al. [10], the lower heat transfer coefficient in vertical downflow can also be explained by the reduction in bubble sliding, which adversely affects heat transfer efficiency by shortening the duration of latent heat transfer.

Fig. 18 also displays the microgravity heat transfer coefficient curve alongside the 1-$g_e$ based heat transfer results for different flow orientations. It is observed that in the low heat flux range, where the heat transfer coefficient exhibits a strong dependency on the wall heat flux, the heat transfer coefficients in microgravity are higher than those of all orientations under Earth gravity. As the heat flux continues to increase, the microgravity heat transfer coefficient decreases below the vertical upflow curve but remains higher than the 45° inclined orientations and vertical downflow curves. After the transition, as indicated with the dotted vertical line, the reduced heat transfer coefficient in microgravity then maintains a steady level without further degradation until reaching the CHF. Notice the microgravity condition is associated with a lower CHF value compared to most of the 1-$g_e$ orientations, except for horizontal flow. The enhancement of microgravity heat transfer coefficient in the low heat flux range can be attributed to the absence of buoyancy in the reduced gravity condition, which leads to earlier bubble nucleation and faster bubble growth compared to terrestrial gravity conditions. Moreover, under microgravity, the generated void fraction is much larger than in the same operating conditions under Earth gravity, resulting in improved heat transfer due to faster flow and intensified turbulence [17]. In contrast, in the higher heat flux range, the greater vapor void fraction in microgravity negatively impacts heat transfer coefficient. This is primarily due to the absence of the buoyancy force in microgravity, which prevents the efficient removal of vapor from the heated section, and in turn, effectively insulates the heated surface. Consequently, wall temperatures increase, and it results in a reduction in heat transfer efficiency. However, even in microgravity condition, bubble nucleation is not fully suppressed, but persists in annular liquid film, preventing further deterioration of average heat transfer coefficient, as shown in Fig. 18.

The influence of flow orientation on heat transfer coefficient varies for different operating conditions. Shown in Fig. 19(a)-(c) are polar plots for average heat transfer coefficient under three different mass velocities, each with three distinct heat fluxes, while maintaining similar system pressure and inlet subcooling conditions. For the lowest $G$ range, Fig. 19(a) clearly exhibits the effect of flow orientation on $h_{tp,avg}$, showing the largest $h_{tp,avg}$ in vertical upflow ($\theta = 90°$) and the lowest $h_{tp,avg}$ in vertical downflow across the entire range of heat flux. As indicated earlier, the superiority of vertical upflow can be attributed to the combined effect of pronounced bubble sliding and efficient vapor removal facilitated by the concurrent direction of the buoyancy force with the flow. Meanwhile, in Fig. 19(a), heat transfer coefficients for horizontal flow and 45° inclined orientations fall between the two extremes of vertical upflow and downflow, resulting in a polar curve resembling an ellipse skewed towards 90°. The effect of flow orientation continues at the intermediate $G$ range of 625.5 ± 43.5 kg/m$^2$s, as depicted in Fig. 19 (b), where a noticeable disparity in $h_{tp,avg}$ is observed between the vertical upflow and the rest of the flow orientations (i.e., the skewness can still be observed). However, as the mass velocity increases further to the range of 826.5 ± 18.5 kg/m$^2$s, as shown in Fig. 19(c), the polar curve exhibits less distorted curvature, indicating inertia around this mass velocity range is effective at attenuating the effects of gravity. Notice the $h_{tp,avg}$ values in Fig. 19(c), at the highest $q''$, showing almost uniform curvature between vertical upflow, $\theta = 90°$, to horizontal flow, $\theta = 0°$, albeit with the small but discernable decrease of $h_{tp,avg}$ for the two downflow orientations. The observed decline in the HTC for the vertical downflow orientation can be attributed to the following factors: (a) Enhanced vapor accumulation within the heated test section, resulting from the upward-directed buoyancy force, which impedes effective vapor flushing, (b) reduced effectiveness in replenishing liquid due to vapor accumulation, consequently elevating wall temperature, (c) reduced sliding of bubbles on the heated wall, leading to shorter durations for latent heat transfer, and (d) diminished effectiveness of turbulent mixing for the downflow configuration, as witnessed from flow visualizations in Figs. 9 and 12.

It is important to recognize the subpar heat transfer performance in horizontal and downward orientations compared to the vertical upflow orientation. This acknowledgement holds significance because several industrial applications employ these flow configurations within their flow loop systems. For instance, in the case of CANDU reactors, the primary coolant flows horizontally along the fuel bundle assembly [29]. Consequently, the asymmetrical flow regime and the associated degradation in heat transfer performance must be considered as a design factor to mitigate postulated accidents such as Loss of Coolant Accidents (LOCA). Moreover, vertical downflow configurations play a vital role in various applications, including U-type tubular heat exchangers used in very high-temperature gas-cooled reactors (VHTR) and downcomer manifolds for offshore satellite platforms [30]. Similar to Earth, the influence of flow orientation is of significant importance in the context of cryogenic space applications. These applications need to be functional not only in microgravity conditions but also in a range of gravitational environments, including reduced gravity levels such as those on the Moon or Mars, or even hypergravity environments as found on planets like Jupiter. Therefore, systems that utilize two-phase flow boiling technologies in these scenarios demand a comprehensive understanding of the impact of flow orientation on two-phase flow and heat transfer performances.

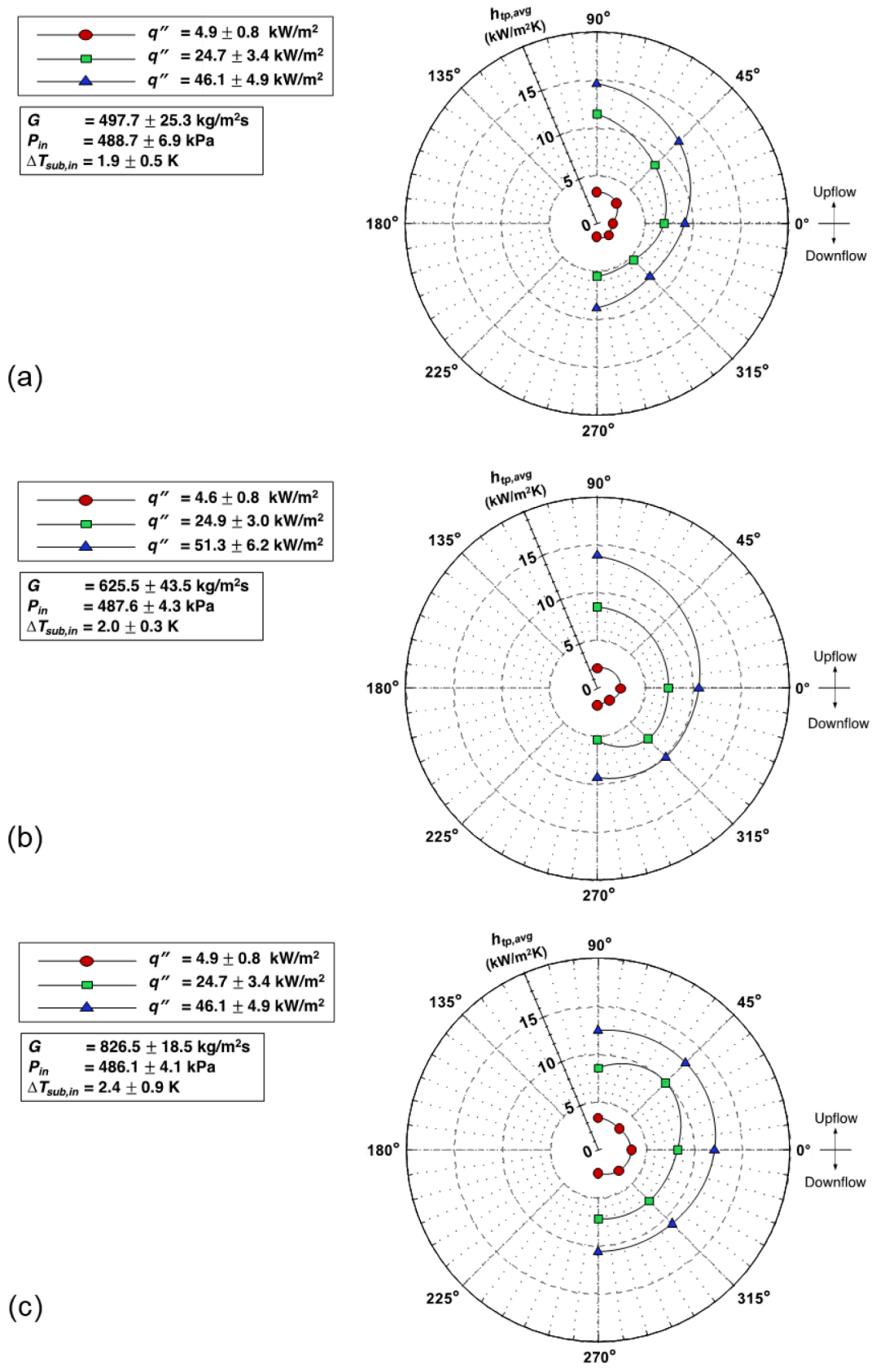


**Fig. 19.** Flow orientation and wall heat flux effects on average heat transfer coefficient at (a) low, (b) intermediate, and (c) high mass velocity.

### 4.3. Mass velocity effects on heat transfer coefficient

#### 4.3.1. Effect of mass velocity on local heat transfer coefficient

Fig. 20 illustrates the variations of the local heat transfer coefficient, $h_{tp,z}$, as the flow quality increases for three distinct ranges of mass velocity (low, intermediate, and high), taking into account three different flow orientations under terrestrial gravity. Flow orientations are denoted by color codes, while different marker shapes indicate the corresponding mass velocity range, as specified in the legend. Note that all the cases analyzed maintain comparable heat flux, inlet pressures, and inlet subcooling conditions, thereby justifying the comparison among the cases. To ensure a fair comparison and minimize potential biases from asymmetric flow patterns, local heat transfer coefficients for the bottom wall are utilized in the case of horizontal flow. Several interesting trends are discerned, highlighting the varying impact of mass velocity on the local heat transfer coefficient, $h_{tp,z}$, contingent upon flow orientation. Particularly noticeable is the pronounced effect of mass velocity on the $h_{tp,z}$ variation observed in the horizontal configuration, where heat transfer coefficients consistently rise with increasing mass velocity across all local flow qualities. In contrast, the $h_{tp,z}$ curves for vertical upflow are much closer to one another over the entire mass velocity range, indicating a diminished impact of mass velocity on vertical upflow boiling. Meanwhile, for vertical downflow, the impact of mass velocity on local heat transfer efficiency is more discernible than for vertical upflow, as evidenced by the ascending trend of $h_{tp,z}$ with increasing mass velocity, specifically from the low $G$ to the intermediate $G$ range. However, notably, the $h_{tp,z}$ curves are closer for the intermediate $G$ to high $G$ range for vertical downflow, indicating a diminished influence of gravity on $h_{tp,z}$ at higher mass flow rates. Clearly, the influence of mass velocity on vertical downflow is significantly weaker compared to the horizontal configuration. This observation establishes horizontal flow as the orientation with the highest susceptibility to the

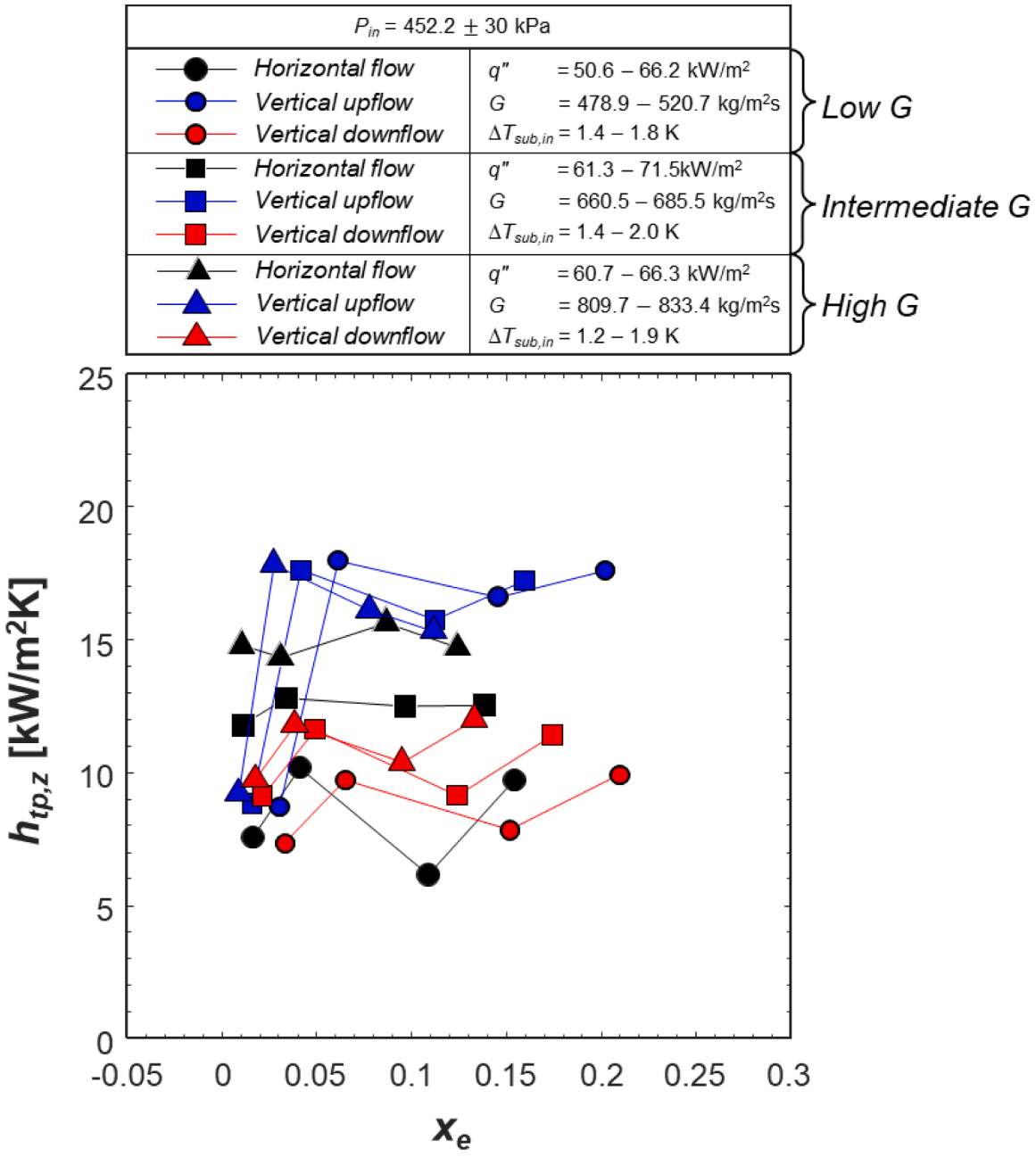


**Fig. 20.** Variation of local heat transfer coefficient with flow quality for three different flow orientations at low, intermediate, and high mass velocities.

impact of mass velocity, while vertical upflow emerges as the orientation least affected by variations in mass velocity.

Another noticeable trend observed in the local heat transfer coefficient curves is the presence of initial spikes specifically in the vertical upflow configuration, which are not as prominent in the other two orientations. Notice the comparable magnitudes of $h_{tp,z}$ between vertical upflow and downflow at flow qualities near zero. However, with a slight increase in flow quality, the $h_{tp,z}$ curves for vertical upflow exhibit a significant escalation, nearly doubling the value of $h_{tp,z}$, whereas the increase in $h_{tp,z}$ for vertical downflow is far less significant. The observed distinct behavior suggests that the flow regime in vertical upflow actively evolves between the flow quality range of 0 and 0.05 due to the explosive activation of bubble nucleation, growth, and detachment at upstream locations. In both the horizontal and vertical downflow configurations, the variation of $h_{tp,z}$ with increasing flow quality is relatively marginal, indicating a subdued transition of the flow regime along the axial direction of the heated tube. For instance, in horizontal flow under the prescribed heat fluxes, the observed flow patterns are primarily stratified annular flow, where the bottom surface is in contact with a relatively thick liquid layer. Therefore, as supported by the flow visualizations depicted in Fig. 10, the sustained bubble nucleation within the liquid film near the bottom wall facilitates a relatively uniform distribution of heat transfer efficiency along the heated length.

#### 4.3.2. *Effect of mass velocity on average heat transfer coefficient*

As captured in Fig. 20, the effect of mass velocity on local heat transfer performance varies with the flow orientation. To assess the global effect of mass velocity on flow boiling performance, the average heat transfer coefficients, $h_{tp,avg}$, for different flow orientation are investigated. In Fig. 21(a)-(d), variations of $h_{tp,avg}$ with increasing heat

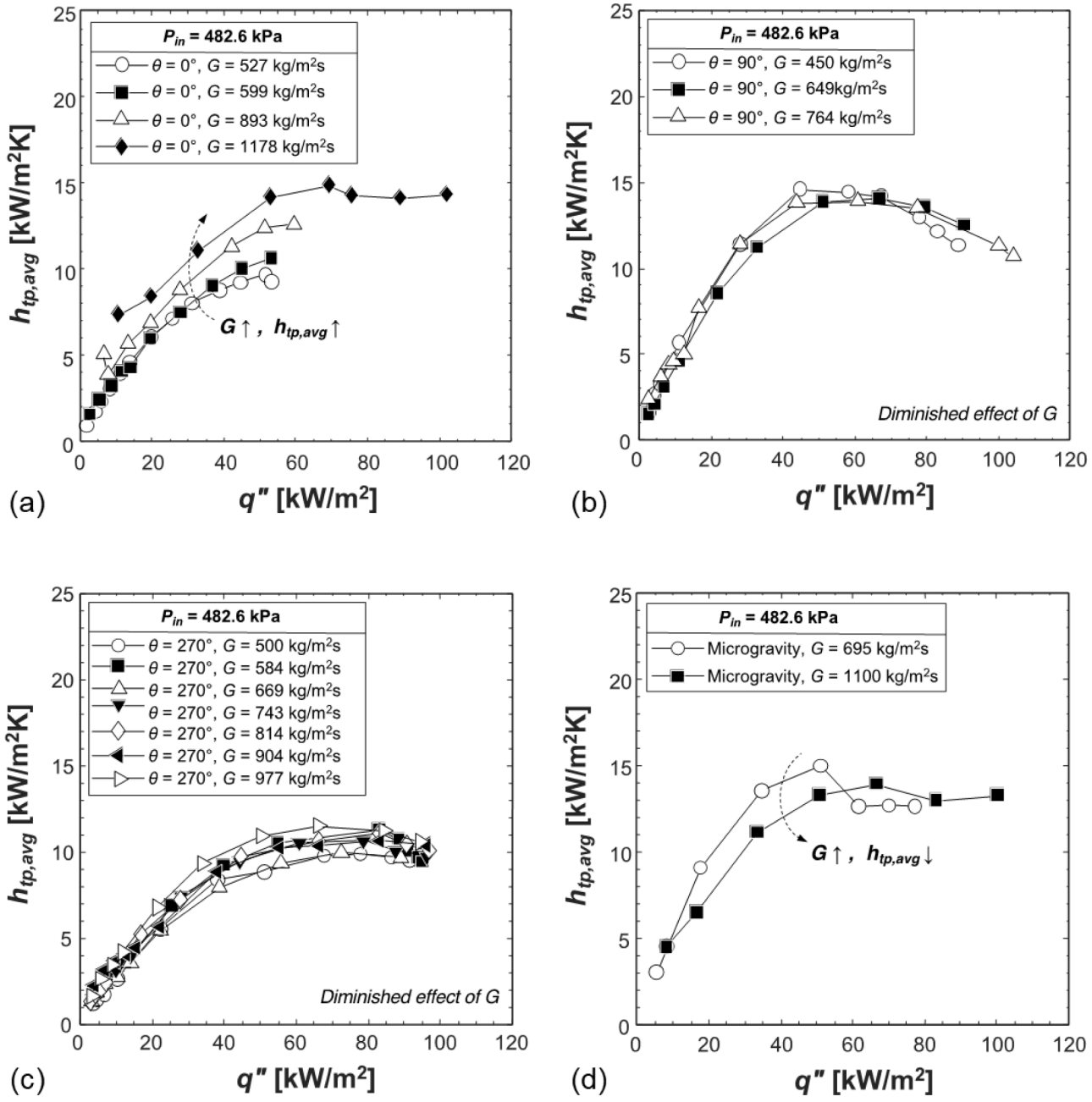


**Fig. 21.** Variation of average heat transfer coefficient with heat flux for multiple mass velocity conditions under the same inlet pressure of 482.6 kPa (70 psi) in (a) horizontal flow, (b) vertical upflow, (c) vertical downflow, and (d) microgravity.

flux are shown for three different flow orientations, along with the microgravity results obtained from the microgravity experiments by Kim et al. [17]. Operating conditions, including the range of varied mass velocities, are provided within the legends for each figure, with all cases corresponding to near saturated inlet ranges of $\Delta T_{sub,in} = 0.8–3.9$ °C

Fig. 21(a) depicts the trend observed in the horizontal flow orientation ($\theta = 0°$), where it clearly shows the monotonic increase of $h_{tp,avg}$ curves with increasing mass velocity. The impact of the mass velocity on the $LN_2$ heat transfer coefficient in the horizontal configuration was also reported by Muller et al. [31]. Based on their experiments, a rough estimation of $h_{tp} \sim \dot{m}^{0.27}$ was suggested, expressing an enhancement of heat transfer coefficient with increasing mass velocity, which aligns with the trend observed in the present study. The observed enhancement in the heat transfer coefficient with increasing mass velocity can be attributed to the observed flow patterns in the horizontal flow orientation. The stratified vapor structures concentrated near the top surface of the heated tube, as presented in Fig. 10, create an asymmetry in the circumferential wall temperature distribution, having higher temperatures at the top wall and lower temperatures at the bottom wall. Consequently, the temperature distribution induces circumferential heat conduction from the top to the bottom, aiming to equalize the temperature difference. As a result of the circumferential heat conduction, the bottom wall temperature rises, leading to a degradation of the heat transfer coefficient for the bottom surface. The degradation of the bottom heat transfer coefficient is more pronounced at lower mass velocities compared to higher mass velocities, primarily due to intensified flow stratification resulting from weaker flow inertia. Conversely, at higher mass velocities due to the enhanced flow inertia, the flow stratification diminishes, leading to a reduction in the effect of circumferential heat conduction. As a result, lower bottom wall temperatures and higher heat transfer coefficients are achieved at higher mass velocity than at low mass velocity, as shown in Fig. 21(a).

The impact of mass velocity on the heat transfer coefficient is significantly suppressed in both the vertical upflow ($\theta = 90°$) and vertical downflow ($\theta = 270°$) configurations, as demonstrated in Fig. 21(b) and 21(c), respectively. This is evident from the overlapping $h_{tp,avg}$ curves for different mass velocity conditions, indicating a diminished effect of mass velocity on the heat transfer performance. Steiner [32] has also reported the limited influence of mass velocity on the flow boiling heat transfer coefficient in vertical upflow, based on investigations with 10 different fluids including cryogenic data for liquid helium from Hilderbrandt [33], as well as data for 9 other conventional room temperature fluids. This suppressed effect of mass velocity on the heat transfer coefficient can be attributed to the dominant nucleate boiling heat transfer mechanism, which is expressed as a function of heat flux and pressure, as highlighted by Kim and Mudawar [34]. Furthermore, the observed flow patterns for both vertical upflow and vertical downflow configurations, as shown in Figs. 8 and 9, and reported visual observations by Thorncroft et al. [10], indicate the pronounced bubble nucleation and bubble lift-off (including bubble sliding) facilitated by buoyancy forces, actively detaching nucleated bubbles from the wall. Persistent bubble nucleation and bubble departure are key components of the nucleate boiling mechanism and are primarily localized phenomena that are less influenced by the bulk liquid temperature or velocity. Steiner [32] also mentioned that fluid motion velocity in the core of the flow has negligible impact on heat transfer on the heated wall, which explains the imperceptible effect of mass velocity on the heat transfer coefficient in vertical upflow and vertical downflow.

Fig. 21(d) depicts the μg $h_{tp,avg}$ trends with increasing heat flux at two different mass velocity conditions, acquired from the parabolic flow boiling experiments by Kim et al. [17]. Here, two interesting trends between the microgravity heat transfer coefficients and mass velocity are observed. Particularly discernable is the downward shift of the μg $h_{tp,avg}$ curve with increasing mass velocity, which clearly indicates degrading heat transfer performance with increasing flow inertia. The second trend to be noticed is the cross-over of the $h_{tp,avg}$ curve of the larger mass velocity over the curve for the lower mass velocity at the higher heat flux region. These two specific trends in the reduced gravity environment has identically been observed by Mudawar et al. [35] from their recent International Space Station (ISS) Flow Boiling and Condensation Experiment (FBCE) using nPFH. The observed trend, in which heat transfer coefficients decreased with increasing mass velocity in a microgravity environment, can primarily be attributed to the significant influence of increasing flow inertia in the absence of buoyancy. In microgravity condition, where the influence of a buoyancy force is negligible, bubble dynamics are primarily governed by interfacial forces, such as interfacial shear and drag induced by phase velocity differences. Consequently, an increase of mass velocity in microgravity directly enhances interfacial shear lift and drag, which facilitates earlier bubble departure and smaller bubble diameters compared to lower mass velocities. The higher frequency of bubble departure and the smaller bubble diameter associated with high mass velocity contribute to a reduced contact time between the bubbles and the heated wall, hindering the effective heat diffusion from the wall to the fluid. Therefore, due to the shortened amount of time for latent heat transfer, overall heat transfer coefficient is deteriorated as mass velocity increases. This observation is intriguing as the effect of mass velocity on vertical upflow or downflow in 1-$g_e$ does not appear to be evident, despite the expectation that increased mass velocity would similarly impact bubble departure frequency and bubble diameters. The key difference lies in the presence of buoyancy in the terrestrial gravity environment. With the continuous presence of buoyancy force under the Earth gravity, bubble departure or lift-off is already actively occurring, thereby limiting the scope for increased mass velocity to further intensify the dynamics.

The findings presented in this study point to the extreme importance of acquiring experimental flow boiling data for cryogenic fluids as a basis for understanding the unique influence of key parameters on heat transfer performance in pursuit of developing empirical correlations and computational models unique to cryogens. Given the extreme sparsity of cryogen data, useful albeit limited understanding of the fluid physics can be derived from prior studies involving other fluids, which may elucidate the type of cryogenic data to be acquired in future experiments. Examples include effects of surface finish [36] and flow instabilities [37].

## 5. Conclusions

The present study explored flow boiling of $LN_2$ in a test section consisting of a circular heated tube for near-saturated inlet conditions. Experiments were performed in five flow orientations: vertical upflow, vertical downflow, horizontal flow, 45° inclined upflow, and 45° inclined downflow, over broad ranges of operating conditions. High-speed video captured interfacial behavior along an adiabatic section situated immediately downstream of the heated test section for all operating conditions, and the resulting images and image sequences provided a basis for explaining the bubble dynamics and dominant flow patterns. The presented heat transfer results primarily focused on investigating the influence of flow orientation on local boiling curves as well as local and average heat transfer coefficients in relation to the flow patterns and interfacial behavior. Key conclusions are:

(1) High-speed video images revealed the following dominant flow regimes for the individual flow orientations: *bubbly – slug – churn – annular* for vertical upflow, *coring bubbly – bubbly – oblong bubbly – annular* for vertical downflow, and *bubbly – plug – stratified annular – annular* for horizontal flow, 45° inclined upflow, and 45° inclined downflow.
(2) Various dynamic parameters of bubbles, such as bubble diameters on the wall, number of bubbles attached to the wall, bubble sliding velocity, and core velocity, were quantified and subjected to analysis. In cases of vertical upflow and downflow

under heat flux percentages exceeding 8 % $q''_{CHF}$, the measured bubble diameters ranged from 0.2 to 0.4 mm. The initial reduction in bubble diameter in the vertical upflow configuration was explained by reference to the classical correlation between bubble frequency and bubble departure diameter as proposed by Zuber [27]. The reduced core velocity observed in the vertical downflow configuration is a clear representation of the impact of the buoyancy force, which impedes the efficient flushing of core vapor in vertical downflow configuration.

(3) An experimental observation of a bubble collision dispersion phenomenon was made under various flow orientations. This observation serves as empirical evidence supporting the existence of this phenomenon in flow boiling, thus corroborating the proposition made by Sharma et al. [28]. The sequence of events associated with this phenomenon was revealed to follow a process of "approach – squeeze – collision – bounce off – disperse".

(4) Intercomparison of the local boiling curves for the different flow orientations revealed the effects of flow orientation on $LN_2$ flow boiling heat transfer characteristics. Linear tangents were drawn to demarcate heat transfer regime transitions.

(5) Comparison of average HTC profiles for the different flow orientations showed a distinct HTC hierarchy, highlighting the superiority of vertical upflow boiling compared to other flow orientations. The disparities among the flow orientations are attributed to the interplay between the buoyancy force vector and flow inertia, which is uniquely discussed for each orientation. As mass velocity increases and exceeds 830 kg/m$^2$s, the disparities in HTC among the orientations become less discernable, underscoring the effectiveness of inertia in mitigating the influence of flow orientation.

(6) Enhanced average HTC was observed in microgravity compared to terrestrial average HTC for all flow orientations, particularly within the low to intermediate heat flux range. The HTC enhancement was attributed to earlier bubble nucleation and faster bubble growth due to the absence of buoyancy force in microgravity. However, the HTC enhancement in microgravity progressively diminished as the heat flux increased, reaching a level between that observed in vertical upflow and vertical downflow.

(7) Varying impacts of mass velocity on HTC were investigated, and the results demonstrated enhanced HTC with increasing mass velocity in horizontal flow, while for vertical upflow and downflow, the effect of mass velocity is significantly diminished. Microgravity HTC decreased with increasing mass velocity, revealing an unexpected and intriguing relation between HTC and mass velocity in the absence of buoyancy force in microgravity.

## Declaration of Competing Interest

The authors declare the following financial interests/personal relationships which may be considered as potential competing interests:

Issam Mudawar reports financial support was provided by NASA.

## Data availability

Data will be made available on request.

## Acknowledgment

The authors are appreciative of the support of the National Aeronautics and Space Administration (NASA) under grants 80NSSC21K0500 and 80GRC018C0055.

## References

[1] W.L. Johnson, J.R. Stephens, NASA's cryogenic fluid management technology development roadmaps, in: Proceedings of the Joint Army-Navy-NASA-Air Force (JANNAF) In-Space Chemical Propulsion Technical Interchange Meeting (TIM), Huntsville, Alabama, 2018.

[2] J. Hartwig, J. Vera, Numerical modeling of the transient chilldown of a cryogenic propellant transfer line, J. Thermophys. Heat Transf. 30 (2016) 1–7.

[3] J. Hartwig, S. Darr, A. Asencio, Assessment of existing two phase heat transfer coefficient and critical heat flux correlations for cryogenic flow boiling in pipe quenching experiments, Int. J. Heat Mass Transf. 93 (2016) 441–463.

[4] M. Meyer, J. Hartwig, S. Sutherlin, A. Colozza, Recent concept study for cryogenic fluid management to support opposition class crewed missions to Mars, Cryogenics (Guildf) (129) (2023), 103622.

[5] M. Mercado, N. Wong, J. Hartwig, Assessment of two-phase heat transfer coefficient and critical heat flux correlations for cryogenic flow boiling in pipe heating experiments, Int. J. Heat Mass Transf. 133 (2019) 295–315.

[6] K. Mishima, H. Nishihara, The effect of flow direction and magnitude on CHF for low pressure water in thin rectangular channels, Nucl. Eng. Des. 86 (1985) 165–181.

[7] H. Zhang, I. Mudawar, M.M. Hasan, Experimental and theoretical study of orientation effects on flow boiling CHF, Int. J. Heat and Mass Transf. 45 (2002) 4463–4477.

[8] C.R. Kharangate, L.E. O'Neill, I. Mudawar, Effects of two-phase inlet quality, mass velocity, flow orientation, and heating perimeter on flow boiling in a rectangular channel: part 1 – two-phase flow and heat transfer results, Int. J. Heat and Mass Transf. 103 (2016) 1261–1279.

[9] S. Saisorn, P. Wongpromma, S. Wongwises, The difference in flow pattern, heat transfer and pressure drop characteristics of mini-channel flow boiling in horizontal and vertical orientations, Int. J. Multiph. Flow 101 (2018) 97–112.

[10] G.E. Thorncroft, J.F. Klausner, R. Mei, An experimental investigation of bubble growth and detachment in vertical upflow and downflow boiling, Int. J. Heat Mass Transf. 41 (1998) 3857–3871.

[11] O. Kawanami, T. Nishida, I. Honda, Y. Kawashima, H. Ohta, Flow and heat transfer on cryogenic flow boiling during tube quenching under upward and downward flow, Microgravity Sci. Technol. 19 (2007) 137–138.

[12] S. Darr, H. Hu, N. Glikin, J.W. Hartwig, A.K. Majumdar, A.C. Leclair, J.N. Chung, An experimental study on terrestrial cryogenic tube chilldown II. Effect of flow direction with respect to gravity and new correlation set, Int. J. Heat Mass Trans. 103 (2016) 1243–1260.

[13] R.J. Simoneau, F.F. Simon, A Visual Study of Velocity and Buoyancy Effects on Boiling Nitrogen NASA Technical Note D-3354, Lewis Research Center, Cleveland Ohio, 1966.

[14] V.V. Klimenko, M.V. Fyodorov, Y.A. Fomichyov, Channel orientation and geometry influence on heat transfer with two-phase forced flow of nitrogen, Cryogenics (Guildf) 29 (1989) 31–36.

[15] V.V. Klimenko, A generalized correlation for two-phase flow heat transfer, J. Heat and Mass Transf. 31 (1988) 541–552.

[16] V. Ganesan, R. Patel, J. Hartwig, I. Mudawar, Review of databases and correlations for saturated flow boiling heat transfer coefficient for cryogens in uniformly heated tubes, and development of new consolidated database and universal correlations, Int. J. Heat Mass Transf. 179 (2021), 121658.

[17] S. Kim, N. Damle, J. Hartwig, I. Mudawar, Cryogenic flow boiling in microgravity: effects of reduced gravity on two-phase fluid physics and heat transfer, Int. J. Heat Mass Transf. 218 (2024), 124751.

[18] S. Kim, N. Damle, J. Hartwig, I. Mudawar, Experimental heat transfer results and flow visualization of horizontal near-saturated liquid nitrogen flow boiling in uniformly heated circular tube under Earth gravity, Int. J. Heat Mass Transf. (2023) in Review.

[19] L.E. O'Neill, R. Balasubramaniam, H.K. Nahra, M.M. Hasan, I. Mudawar, Flow condensation heat transfer in a smooth tube at different orientations: experimental results and predictive models, Int. J. Heat Mass Transf. 140 (2019) 533–563.

[20] E.W. Lemmon, M.L. Huber, M.O. McLinden, NIST standard reference database 23: reference fluid thermodynamic and transport properties-REFPROP, Version 10.0, Gaithersburg, Maryland, 2018.

[21] M. Blander, J.L. Katz, Bubble nucleation in liquids, AlChE J. 21 (1975) 833–848.

[22] D. Bogojevic, K. Sefiane, G. Duursma, A.J. Walton, Bubble dynamics and flow boiling instabilities in microchannels, Int. J. Heat Mass Transf. 58 (2013) 663–675.

[23] T. Oshinowo, M.E. Charles, Vertical two-phase flow Part I. flow pattern correlations, Canadian J. Chem. Eng. 52 (1974) 25–35.

[24] S. Kim, J. Lee, J. Hartwig, I. Mudawar, Computational investigation of vertical upflow boiling of liquid nitrogen and effects of bubble collision dispersion force, Int. J. Heat Mass Transf. 203 (2023), 123780.

[25] N.T. van Dresar, J.D. Siegwarth, Near-horizontal, two-phase flow patterns of nitrogen and hydrogen at low mass and heat flux, NASA technical memorandum, NASA-TP-2001-210380-CD, (2001).

[26] C. Hutter, A. Sanna, T.G. Karayiannis, D.B.R. Kenning, R.A. Nelson, K. Sefiane, A. J. Walton, Vertical coalescence during nucleate boiling from a single artificial cavity, Exp. Therm. Fluid Sci. 51 (2013) 94–102.

[27] M. Zuber, Hydrodynamic Aspects of Boiling Heat Transfer, University of California at Los Angeles, 1959. USAEC Report, AECU-4439PhD thesis1959.

[28] S.L. Sharma, T. Hibiki, M. Ishii, C.S. Brooks, J.P. Schlegel, Y. Liu, J.R. Buchanan, Turbulence-induced bubble collision force modeling and validation in adiabatic two-phase flow using CFD, Nucl. Eng. Des. 312 (2017) 399–409.

[29] B.N. Hanna, CATHENA: a thermal hydraulic code for CANDU analysis, Nucl. Eng. Des. 180 (1998) 113–131.

[30] K. Usui, K. Sato, Vertically downward two-phase flow, J. Nucl. Sci. Technol. 26 (1989) 670–680.
[31] H.M. Muller, W. Bonn, D. Steiner, Heat transfer and critical heat flux at flow boiling of nitrogen and argon within a horizontal tube, in: Proceedings of the Advanced Course in Heat Exchangers: Theory and Practice. ICHMT Symposium, 1981, pp. 233–250.
[32] D. Steiner, Heat transfer during flow boiling of cryogenic fluids in vertical and horizontal tubes, Cryogenics (Guildf) 26 (1986) 309–318.
[33] G. Hildebrandt, Der Wärmeübergang an Siedendes Helium I bei Erzwungener Strömung im Senkrechten Rohr, Technische Universität, Berlin, 1971. PhD Thesis.
[34] S. Kim, I. Mudawar, Review of databases and predictive methods for heat transfer in condensing and boiling mini/micro-channel flows, Int. J. Heat Mass Transf. 77 (2014) 627–652.
[35] I. Mudawar, V.S. Devahdhanush, S.J. Darges, M. Hasan, H. Nahra, R. Balasubramaniam, J.R. Mackey, Heat transfer and interfacial flow physics of microgravity flow boiling in single-side-heated rectangular channel with subcooled inlet conditions – Experiments onboard the International Space Station, Int. J. Heat Mass Transf. 207 (2023), 123998.
[36] G. Liang, I. Mudawar, Review of channel flow boiling enhancement by surface modification, and instability suppression schemes, Int. J. Heat Mass Transf. 146 (2020) 533–563.
[37] L.E. O'Neill, I. Mudawar, Review of two-phase instabilities in macro- and micro-channel systems, Int. J. Heat Mass Transf. 157 (2020), 119738.